On the breakup of fluid films of finite and infinite extent

Javier A. Diez[a)]
Instituto de Física Arroyo Seco, Universidad Nacional del Centro de la Provincia de Buenos Aires, Pinto 399, 7000, Tandil, Argentina

Lou Kondic[b)]
Department of Mathematical Sciences, Center for Applied Mathematics and Statistics, New Jersey Institute of Technology, Newark, New Jersey 07102, USA

(Received 16 November 2006; accepted 24 May 2007; published online 19 July 2007)

We study the dewetting process of thin fluid films that partially wet a solid surface. Using a long-wave (lubrication) approximation, we formulate a nonlinear partial differential equation governing the evolution of the film thickness, h. This equation includes the effects of capillarity, gravity, and an additional conjoining/disjoining pressure term to account for intermolecular forces. We perform standard linear stability analysis of an infinite flat film, and identify the corresponding stable, unstable, and metastable regions. Within this framework, we analyze the evolution of a semi-infinite film of length L in one direction. The numerical simulations show that for long and thin films, the dewetting fronts of the film generate a pearling process involving successive formation of ridges at the film ends and consecutive pinch-off behind these ridges. On the other hand, for shorter and thicker films, the evolution ends up by forming a single drop. The time evolution as well as the final drops pattern show a competition between the dewetting mechanisms caused by nucleation and by free surface instability. We find that precise computations, requiring quadrupole precision of computer arithmetic, are often needed to avoid spurious results. © *2007 American Institute of Physics*. [DOI: 10.1063/1.2749515]

I. INTRODUCTION

The evolution of partially wetting thin liquid films on solid substrates and the subsequent pattern formation are a subject of growing importance. This type of flow is of widespread relevance in a variety of technological applications, ranging from various types of coatings[1–3] to new applications in micro- and nanofluidics.[4,5] These films are often unstable and could break up, leading to the formation of dry spots that are often undesirable. One important question is, what are the mechanisms involved in the dewetting and breakup of unstable thin films?

Numerous theoretical, computational, and experimental works have addressed this question, and in our brief introduction we discuss only a few works that are closely related to the topic of this paper. By now it has been generally accepted that there are basically two instability mechanisms (see Ref. 6 for a brief review of relatively recent developments). These two mechanisms are (i) free surface instability, sometimes also called spinodal instability due to the similarity to spinodal decomposition of a binary mixture,[7] described by the Cahn-Hilliard equation,[8] and (ii) nucleation-type instability (or simply nucleation), which is due to the presence of defects of either the film or the solid surface. It is often unclear which of these two mechanisms is relevant in a particular experiment, and only during the past decade or so has a more precise understanding of this problem been reached.[9–21]

An important ingredient in all problems involving dewetting is the model of liquid-solid interaction (see Refs. 22 and 23 for reviews). Using one of the approaches, the so-called diffuse interface model,[24] recent theoretical works have discussed in some detail the two instability mechanisms mentioned above.[25–28] In particular, in these works it is shown that both regimes may appear during the evolution of a localized perturbation. In the surface instability dominated regime, lateral and traveling undulations develop at both sides simultaneously with the growth of the initial perturbation, leading to patterns whose distance is on average close to the wavelength of maximum growth, λ_m, resulting from the linear stability analysis (LSA) of the response of a film to infinitesimal perturbations. On the other hand, in the nucleation-dominated regime, the initial disturbance grows and expands laterally while rims are formed at both sides. The final structure is a set of drops (connected by thin films) separated by an average distance unrelated to the wavelength of maximum growth of the surface instability. Related discussion can be found in other experimental and theoretical works (e.g., Refs. 11, 12, 14, 16–18, and 21) that have considered similar problems. However, it is worth pointing out that, to our knowledge, the mechanism that determines the distance between the drops in the nucleation-dominated regime is not well understood.[10,11,15–17,21,26,29–32] Particularly in the experiments, an additional complication is that multiple nucleation centers exist and therefore the emerging wavelengths depend not only on the instability properties of a film, but also on the properties of the substrate and more generally on the conditions under which the experiments are performed (see Ref. 16 and references therein for a review of this issue). Some progress has been reached recently by con-

[a)]Electronic mail: jdiez@exa.unicen.edu.ar
[b)]Electronic mail: kondic@njit.edu

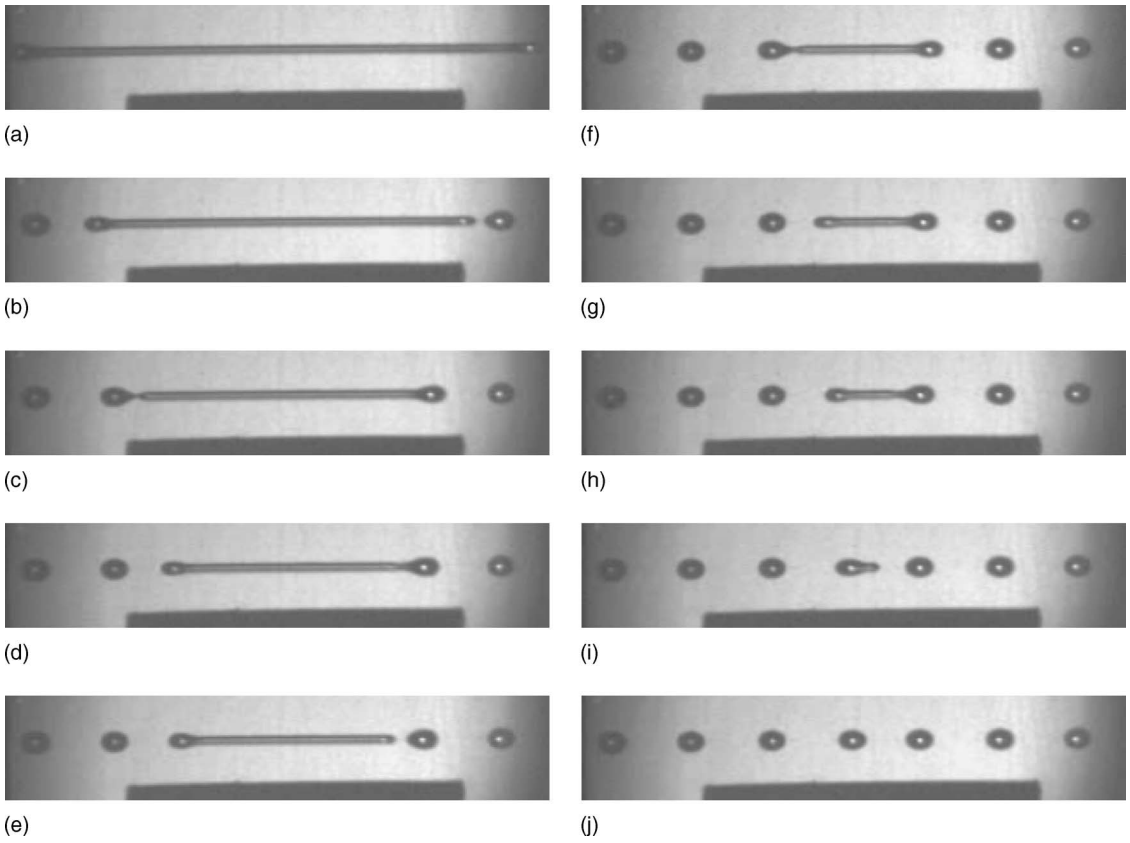

FIG. 1. Evolution of a fluid strip (PDMS, viscosity $\nu=20St$, surface tension $\gamma=19.8$ dyn/cm) on a glass substrate previously coated with a fluorinated solution (Ref. 39). The equilibrium contact angle is 57° and the black segment corresponds to 4.1 cm.

sidering the details of the film profiles before the breakup (so-called "satellite-hole" formation[15–19,21,33]).

All the works listed so far discuss the instability of *infinite* two-dimensional (2D) or 3D liquid films. However, practical problems commonly involve films and rivulets of finite extent, in particular in a variety of printing-related applications such as direct printing for microcircuit production,[34] and so-called microcontact printing.[35,36] These processes are known to be subject to instabilities[37,38] and, furthermore, experimental results clearly point out that the presence of fronts has a strong influence on the instability development.

Figure 1 shows an example of experiments where the end effects are clearly important. This figure shows breakup and pearling process of a long thin fluid rivulet placed on a partially wetting substrate.[39] The ends of the rivulet dewet along its axis toward the center while the long side contact lines remain straight and at rest. At the rivulet ends, ridges of increasing size develop. The width of the necks connecting the ridges and the main body of the rivulet decreases until a drop detaches at each end. As the axial dewetting process continues, successive ridges and neck breakups give place to a nearly equidistant linear array of drops.

A problem that is similar to the one shown in Fig. 1 (at least on the level of experimental photographs) is the breakup of an initially extended drop in an otherwise quiescent fluid.[40–42] Features such as the formation of bulges at the extremes, rupture of the neck connecting a bulge to the main drop, and drop detachments appear similar in both problems. Physically, however, the drop breakup problem differs significantly from the breakup of a rivulet, since there is no solid surface involved and, therefore, solid-liquid interaction including the contact lines is absent. However, both problems involve pinch-off of liquid drops at the fluid fronts, and therefore one may expect that some concepts that were useful in understanding the breakup of a liquid drop could also be appropriate in the rivulet context. We note that in the elongated drop problem, the final pattern of drops is mainly controlled by the ratio of the ambient fluid and drop viscosities. In the problem illustrated by Fig. 1, however, the wettability properties of the substrate are important.

In the present paper, we concentrate on the role of finite size of liquid films on instability development in the simplified geometry that considers a film of finite extent in the rivulet direction (x axis), but infinite in the other one. Therefore, we ignore the transverse curvature that is clearly of importance in the experiments such as those presented in Fig. 1. Even in this simplified geometry, we find new and interesting results regarding the influence of finite film size, and expect that these results will be crucial for understanding the breakup of 3D fluid strips. That problem will be considered in detail in future work.

We perform the study by numerically solving the governing nonlinear equation for the film thickness within the lubrication approximation, including capillary effects, gravity, as well as partial wetting via a disjoining pressure model.

Although this work mostly concentrates on finite films, we also discuss the breakup of infinite ones and the properties of the resulting patterns. An additional motivation for considering infinite films is that we find that some important aspects of *finite* film dynamics could be understood using the concepts developed for the simpler case of infinite films.

This paper is organized as follows. Section II presents the basic mathematical model. The linear stability analysis of an infinite film is presented in Sec. III, where we also discuss the stability under finite amplitude perturbations, related to film metastability. Section IV discusses finite films. Here, we also discuss, compare, and interpret some of the results obtained for the finite films in terms of those obtained for infinite ones. Appendixes A and B discuss the disjoining pressure model and some details of the steady single drop solution, respectively.

II. LUBRICATION MODEL

In the study of thin film flows on solid substrates, the evolution of the fluid thickness, h, is typically described under the framework of lubrication theory. This approach allows us to reduce Navier-Stokes equations to a single nonlinear partial differential equation for h. In addition, finite contact angles can be included in the model by accounting for van der Waals forces, as described below. We note that although lubrication theory is strictly valid only in the problems characterized by vanishing free surface slopes, it has been used commonly in partial wetting conditions, therefore in situations in which the contact angle is not necessarily small;[43–45] see also Refs. 24 and 46–48 for further discussion regarding involved issues. This approach has been justified in part by the works that show that even in the case of large contact angles, only relatively small deviations from more complete models result. For example, Ref. 49 compares the solutions for the cross section of a rivulet flowing down a plane obtained by solving the complete Navier-Stokes equation with the predictions of the lubrication approximation (see their Table I). For a contact angle of 30°, they find that the differences between the two approaches related with the shape of the free surface are of the order of a few percent. Although the accuracy of the lubrication approximation is not so good regarding the details of the velocity field, they find that these velocity differences cancel out when the total flux along the rivulet is computed. The issue of appropriateness of the use of the lubrication approximation was also discussed earlier.[50] In that work, it was shown that there are some differences in the free surface slope between lubrication theory and Stokes formulation, but only very close to the contact line.

Another concern regarding the use of the lubrication approximation is that one typically (as we do here) approximates curvature of the free surface by h_{xx}, where x is an in-plane coordinate. This issue was considered in Ref. 51, where it is shown that use of the complete nonlinear curvature yields only a few percent difference [see, e.g., Fig. 2(b) in Ref. 51]. There have been also some attempts[52,53] to improve the typical lubrication approximation approach. These works show that including a correction factor to the flux term in the continuity equation extends the limits of its validity. Therefore, it may be appropriate to implement these improvements when precise quantitative results are desired. In the present problem, where we are mainly concerned with the basic mechanisms involved in the dewetting and breakup processes, we expect that the standard lubrication approach is sufficient.

The van der Waals forces are included in the formulation of a lubrication model via disjoining pressure $\Pi(h)$ (see Appendix A). The resulting equation for the fluid thickness, h, is (see, e.g., Refs. 43, 44, and 54)

$$3\mu\frac{\partial h}{\partial t}+\gamma\nabla\cdot(h^3\nabla\nabla^2 h)+\nabla\cdot[h^3\nabla\Pi(h)]-\rho g\nabla\cdot(h^3\nabla h)=0, \tag{1}$$

where μ is the viscosity, ρ is the fluid density, and g is the gravity. Here, the first term stands for viscous dissipation and the other three terms account for the driving forces, which are surface tension, van der Waals, and gravity force, respectively. The disjoining pressure model that we use,

$$\Pi(h)=\kappa f(h)=\kappa\left[\left(\frac{h_*}{h}\right)^n-\left(\frac{h_*}{h}\right)^m\right],$$

introduces κ (proportional to the Hamaker constant) and the exponents $n>m>1$ [note that $f(h)$ is a dimensionless function]. The first term represents liquid-solid repulsion, while the second term is attractive, leading to a stable film thickness $h=h_*$ (related to precursor film thickness, see Appendixes A and B). Within this model, $\kappa=S/(Mh_*)$, where S is the spreading parameter, and $M=(n-m)/[(m-1)(n-1)]$ (see Appendix A). The spreading parameter can be related to the apparent contact angle θ via Laplace-Young condition $S=\gamma(1-\cos\theta)$.

By defining the dimensionless variables $\hat{h}=h/h_c$, $\hat{x}=x/x_c$, $\hat{y}=y/x_c$, $\hat{t}=t/t_c$, with

$$t_c=\frac{3\mu}{\gamma}\frac{x_c^4}{h_c^3},$$

Eq. (1) becomes

$$\frac{\partial h}{\partial t}+\nabla\cdot(h^3\nabla\nabla^2 h)+K\nabla\cdot[h^3 f'\nabla h]-D\nabla\cdot(h^3\nabla h)=0, \tag{2}$$

where $f'=df/dh$ and we have omitted the "hat" symbol for simplicity. The dimensionless constants are given by

$$D=G\frac{x_c^2}{a^2},\quad K=\frac{\kappa}{\gamma}\frac{x_c^2}{h_c}, \tag{3}$$

with $a=\sqrt{\gamma/\rho g}$ being the capillary length. We use $G=1$ when gravity effects are considered and $G=0$ when they are neglected. From now on we take capillary length as the length scale, so that $h_c=x_c=a$. Thus, we have $D=G$ and $K=(1-\cos\theta)/(Mh_*)$ with h_* in units of a. We restrict ourselves here to the two-dimensional planar case, so that Eq. (2) reduces to

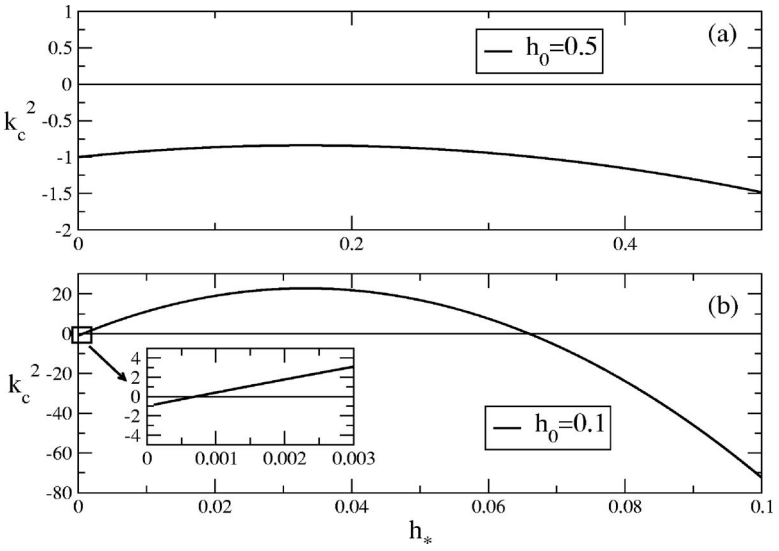

FIG. 2. Square of the critical wave number, k_c^2, as a function of h_* for (a) $h_0=0.5$, (b) $h_0=0.1$ (the inset shows the region for very small h_*). Here $G=1$, $n=3$, $m=2$, and $\theta=50°$ (we use these parameters in what follows except when stated otherwise).

$$\frac{\partial h}{\partial t}+\frac{\partial}{\partial x}\left[h^3\left(\frac{\partial^3 h}{\partial x^3}+Kf'\frac{\partial h}{\partial x}-G\frac{\partial h}{\partial x}\right)\right]=0. \tag{4}$$

This is the equation that we analyze in the rest of the paper.

Remark. We note that although we base our length scales x_c and h_c on the capillary length, a, our results are relevant to a wide range of film thicknesses including micrometric or nanometric films. Interested readers can simply replace the length scales as appropriate to the problem in question. It should be noted that some physical effects become more or less important for different films; e.g., for very thin films, gravity loses its importance, as can be seen from the definition of D.

We also note that in what follows, we mostly use the values of h_* in the range $[0.001, 0.01]$. For films of thickness comparable to the capillary length, this choice leads to a relatively thick precursor film (on a micrometer scale). Precise comparison to experiments would require carrying out computations with a thinner precursor, which carries a substantial increase in the computational cost. However, the linear stability results that follow in Sec. III A can easily be extended to smaller values of h_*, if so desired.

III. UNIFORM INFINITE FILM

We present here an overview of the standard linear stability analysis (LSA) of an infinite film of uniform thickness. Some related results, although for different disjoining pressure models, can be found in Refs. 26 and 27. We will see that the analysis of infinite films sets a convenient framework to characterize the dynamics of finite length films discussed later in Sec. IV.

A. Linear stability analysis of an infinite film

In order to study the stability of a uniform solution, we perturb it by setting $h=h_0+\epsilon h_0 e^{ikx+\beta t}$, where $k=2\pi/\lambda$ is the wavenumber, β is the growth rate, and $\epsilon \ll 1$ is the amplitude. Upon replacing this expression into Eq. (4), and considering only $O(\epsilon)$ terms, we obtain

$$\beta=h_0^3k^2(k_c^2-k^2), \tag{5}$$

where

$$k_c^2=-G+Kf'(h_0)=-G-\frac{K}{h_0}\left[n\left(\frac{h_*}{h_0}\right)^n-m\left(\frac{h_*}{h_0}\right)^m\right]. \tag{6}$$

If $k_c^2<0$, we have $\beta<0$ and the film is linearly stable for all k. On the other hand, if $k_c^2>0$, the range $0<k<k_c$ leads to instability. Figure 2 shows k_c^2 as a function of h_* for two values of h_0, and for $G=1$, $n=3$, $m=2$, and $\theta=50°$ (we use these parameters in what follows except otherwise stated; the value of the contact angle is motivated by the experiments shown in Fig. 1). We see that when the fluid film is thick enough [e.g., $h_0=0.5$ as in Fig. 2(a)], the film is stable for all h_*. For relatively small h_0, there is a range $h_*^-<h_*<h_*^+$ leading to instability. The fact that van der Waals forces cannot destabilize the film for h_* less than a threshold value, h_*^-, is due to the fact that the range of the intermolecular forces is then too short in order to drive the instability of the bulk. On the other hand, the film also cannot be destabilized by van der Waals forces for h_* greater than a certain value h_*^+ due to the stabilizing effect of gravity. For $h_*>h_0$, both gravity and intermolecular forces stabilize the film.

Specifically, for $n=3$ and $m=2$, we have $K=2(1-\cos\theta)/h_*$ and the condition $k_c^2=0$ reduces to a quadratic equation, whose roots are

$$h_*^{\pm}(h_0)=\frac{h_0}{3}\left[1\pm\sqrt{1-\frac{3Gh_0^2}{2(1-\cos\theta)}}\right]. \tag{7}$$

Figure 3 shows these two solutions for $G=1$, which together determine the region of instability in the (h_*,h_0) plane. We notice that if

$$h_0>h_{0,cr}=\sqrt{\frac{2(1-\cos\theta)}{3}}, \tag{8}$$

the film is linearly stable for any h_*.

We note in passing that although this result may appear different from the one obtained when using the diffuse inter-

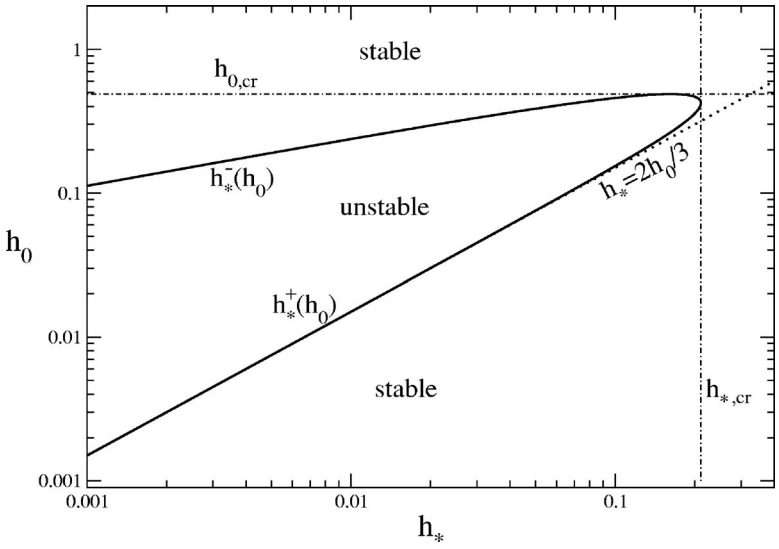

FIG. 3. Curve of marginal stability (solid line) as given by Eq. (7) for $G=1$. The dash-dotted lines correspond to Eqs. (8) and (9), respectively, and the dotted line is $h_*=2h_0/3$.

face potential (see, e.g., Ref. 26), the difference lies only in the choice of parameters. Considering next the maximum of the curve $h_*^+(h_0)$, we find that for

$$h_* > h_{*,\mathrm{cr}} = \sqrt{\frac{1-\cos\theta}{2}}, \tag{9}$$

the film is stable for any value of h_0, analogously to the diffuse interface potential.[26]

Note that for $G=0$, the roots of Eq. (7) collapse to $h_*^-=0$ and $h_*^+=2h_0/3$, also shown in Fig. 3. Thus, without gravity, the film is unstable in the range $0<h_*<2h_0/3$ for any h_0.

Within the unstable region, the dispersion relation, Eq. (5), gives maximum growth rate

$$\beta_m = \tfrac{1}{4}h_0^3 k_c^4, \tag{10}$$

at the wavenumber

$$k_m = \frac{2\pi}{\lambda_m} = \frac{k_c}{\sqrt{2}}.$$

We note that Eq. (10) shows a strong dependence of β on h_0. In addition, variation of h_* for fixed h_0 can also lead to a wide range of β's. To illustrate this, Fig. 4 shows $\beta(k)$ for $h_0=0.1$ and two different values of h_*. Note that one order of magnitude variation on h_* yields a ratio of maximum growth rates close to 10^3. Furthermore, smaller h_* leads to instability at significantly longer wavelengths. We will use these results to compare to the numerical simulations that follow.

We mostly focus our study on a given pair of exponents (n,m), that is, $e_0=(3,2)$. However, other values can be used to account for different types of intermolecular interactions. Thus, we show briefly the effect of varying (n,m), concentrating on $e_1=(4,3)$ and $e_2=(9,3)$, which have been used extensively in the literature (see, e.g., Refs. 43, 55, and 56). Figure 5 shows that as the exponents vary from e_0 to e_2, the unstable region for $G=1$ becomes narrower with larger values of both $h_{*,\mathrm{cr}}$ and $h_{0,\mathrm{cr}}$. For $G=0$, Eq. (6) shows that the unstable range reduces to $0<h_*<(m/n)^{n-m}h_0$.

Let us now consider the effect of contact angle, θ. Figure 6 shows that the unstable area, as well as the corresponding value of $h_{0,\mathrm{cr}}$, decreases as θ decreases, which implies that the unstable region collapses as $\theta\to 0$, i.e., the film is stable for a completely wetting fluid.

B. Absolute stability analysis

In this section, we analyze the absolute stability of an infinite film by discussing the Gibbs free energy of the system, following the approach put forward recently.[7,26,57] We give a short overview of this approach applied to the disjoining pressure model outlined in Appendix A.

A linearly stable uniform film is absolutely stable (to finite amplitude perturbations) only if there is no thickness profile with smaller energy. Otherwise, under finite perturbations, the uniform state h_0 evolves to a nonuniform configuration; this state is called metastable.

Let us assume that in a domain $(0,X)$, the film is flat everywhere except in a finite region of length L where there

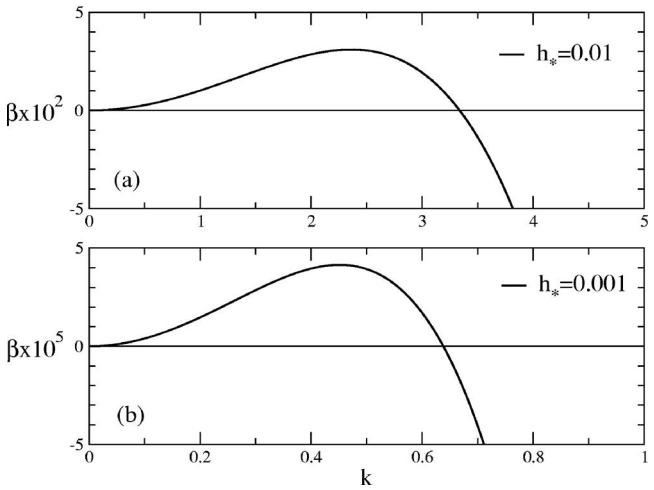

FIG. 4. Dispersion relation $\beta(k)$ for $h_0=0.1$ and (a) $h_*=0.01$, (b) $h_*=0.001$.

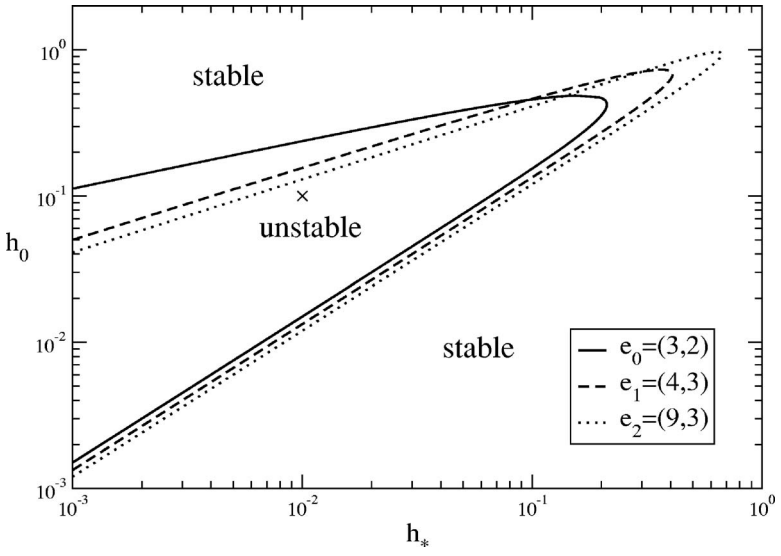

FIG. 5. Curves of marginal stability for $\theta=50°$ and different pairs of exponents (n,m). The cross corresponds to the case $(h_*,h_0)=(0.01,0.1)$, discussed later in the text.

is a higher (or lower) plateau of thickness h_0 with transition regions of negligible width with respect to L. The equilibrium configuration of the system must minimize the free energy

$$E=\int_0^X \left[\frac{h_x^2}{2}+\omega(h)+G\frac{h^2}{2}\right]dx, \tag{11}$$

with the constraint of constant area, defined by $A=\int_0^X h dx$. Here, $\omega(h)$ is the (nondimensional) energy density due to van der Waals forces given by [see Eq. (A6) for the dimensional version]

$$\omega(h)=Ku(h)+s, \tag{12}$$

where $s=S/\gamma=1-\cos\theta$, and

$$u(h)=h_*\left[\frac{1}{n-1}\left(\frac{h_*}{h}\right)^{n-1}-\frac{1}{m-1}\left(\frac{h_*}{h}\right)^{m-1}\right]. \tag{13}$$

We note that the use of a more complex form for disjoining pressure may lead to $\omega=\omega(h,h_x,\ldots)$.[58–61] Minimizing the free energy is equivalent to minimizing the functional

$$\mathcal{F}=\int_0^X \left[\frac{h_x^2}{2}+Ku(h)+s+G\frac{h^2}{2}-p(\bar{h})h\right]dx, \tag{14}$$

where p is a Lagrange multiplier. Note that p is also the dimensionless pressure corresponding to an equilibrium flat configuration of thickness $\bar{h}=A/X$. In fact, by setting $\partial h/\partial t=0$ in Eq. (4) and integrating twice, we obtain

$$p(\bar{h})=-Kf(\bar{h})+G\bar{h}$$

for a uniform film of thickness $\bar{h}$ (see also Appendix B).

By neglecting the energy in the narrow transition regions at the extremes of the plateau region of thickness h_0 and length L, the energy per unit length can be calculated from Eq. (14) as

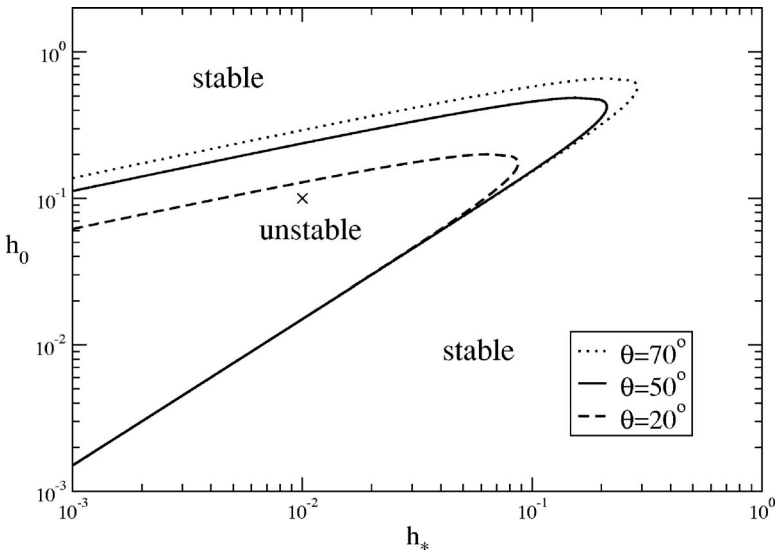

FIG. 6. Curves of marginal instability for $(n,m)=(3,2)$ and different contact angles θ. The cross corresponds to the case $(h_*,h_0)=(0.01,0.1)$.

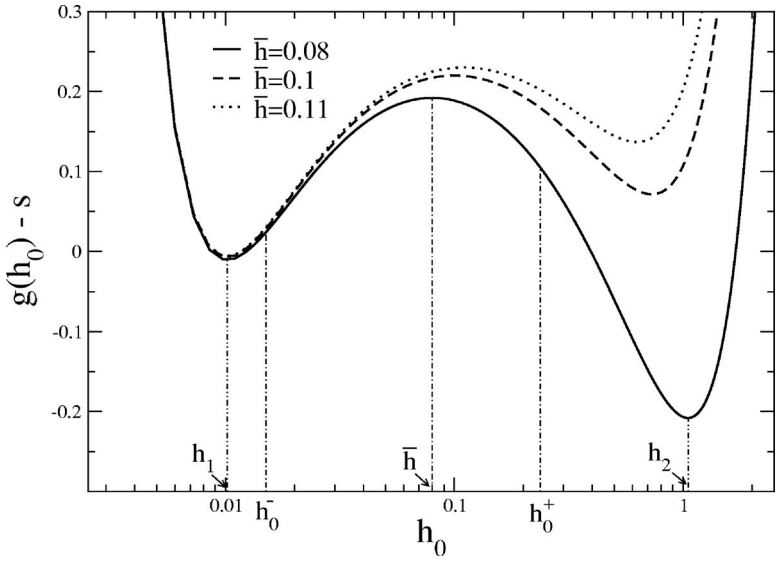

FIG. 7. Energy per unit length, $g(h_0)-s$, as a function of plateau thickness, h_0, for $h_*=0.01$ and different average thicknesses $\bar{h}$. The values of h_0 at the inflection points and at minimum and maximum points are marked for $\bar{h}=0.08$.

$$g(h_0) = Ku(h_0) + s + G\frac{h_0^2}{2} - p(\bar{h})h_0.$$

Figure 7 shows the values of h_0 that lead to local minima of $g(h_0)$ for given $\bar{h}$. Note that the inflection points of these curves satisfy

$$\frac{d^2g}{dh_0^2} = -K\frac{df}{dh_0} + G = 0,$$

a condition that is coincident with $k_c^2=0$ as given by Eq. (6). Consequently, the two inflection points (marked h_0^- and h_0^+ in Fig. 7) represent the lower and upper linearly stable thicknesses. As a matter of fact, $h_0=\bar{h}$ also satisfies $dg/dh_0=0$, and it is a local maximum of $g(h_0)$.

The two minima of $g(h_0)$, h_1 ($\approx h_*$), and h_2 correspond to absolutely stable film thicknesses, and are specified by

$$\frac{dg}{dh_0} = K\frac{du}{dh_0} + Gh_0 - p(\bar{h}) = -Kf(h_0) + Gh_0 - p(\bar{h}) = 0.$$

The metastable thickness range is limited by the values of h_0 where the two minima have the same energy and the same pressure (see Ref. 26 for details). Therefore, the upper and lower limits of h_0, namely h_1 and h_2, as well as $\bar{h}$ are given by the roots of

$$\left.\frac{dg}{dh_0}\right|_{h_1} = 0,$$

$$\left.\frac{dg}{dh_0}\right|_{h_2} = 0,$$

$$g(h_1) = g(h_2).$$

Figure 8 shows the values of h_1 and h_2 that define a

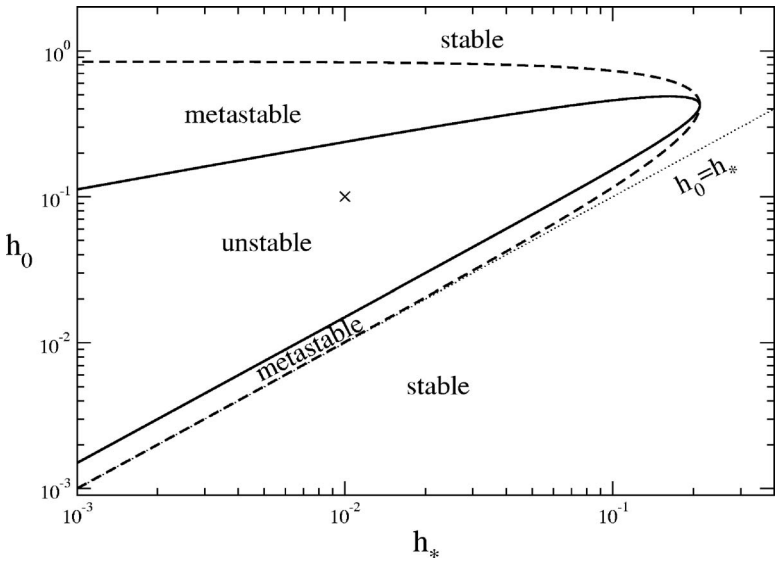

FIG. 8. Regions of stability, metastability, and linear instability of infinite flat films in the parameter space (h_*,h_0). The cross indicates the typical case $(h_*,h_0)=(0.01,0.1)$.

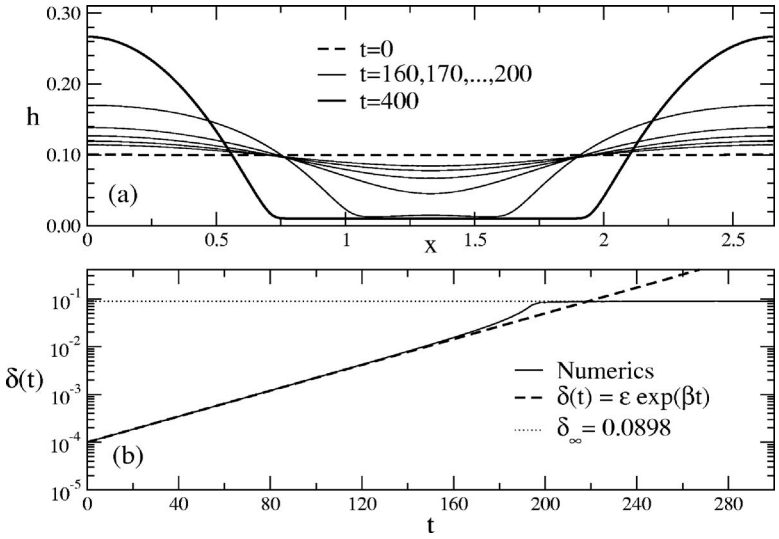

FIG. 9. Evolution of an *unstable* infinite film for $h_0=0.1$, $h_*=0.01$, and $\epsilon=10^{-3}$.

metastable regime in (h_*,h_0) space (dashed line in Fig. 8). In Sec. IV, we use this diagram as a framework to describe the results of the evolution of a uniform film of *finite* length.

Note that the lower boundary of the metastable regime shown in Fig. 8 is either coincident or above the line $h_0=h_*$ (dotted line in Fig. 8). Therefore, infinite films thinner that h_* are absolutely stable for any perturbation.

C. Computational results for infinite films

Here we discuss the stability of infinite films via numerical simulations, and compare the results to the LSA from Sec. III A. The details of our computational method are given in Ref. 62; a very brief outline follows here.

The computational domain $(0\leqslant x\leqslant X)$ is divided into n_x cells of size Δx centered at node points x_i $(i=1,\ldots,n_x)$. Equation (4) is then discretized in space by using a central finite-difference scheme, while time discretization is performed by employing an implicit Crank-Nicolson method. The time step is controlled by imposing a tolerance equal to 10^{-3} of the maximum relative error.[62] Regarding spatial resolution, we use $\Delta x=0.01$, which yields converged results.

To compare to the LSA, we carry out the computations for a uniform film of thickness h_0, which is perturbed as follows:

$$h(x,0)=h_0[1+\epsilon\cos(2\pi x/\lambda)], \tag{15}$$

with $\epsilon=10^{-3}$. The numerical simulation is performed using $h_x=h_{xxx}=0$ at $x=0,X$, which leads to no-flow conditions across the domain boundaries. Thus, by using $X=n\lambda$, with n an integer, these conditions function as periodic boundary conditions and are consistent with the assumption of an infinite film.

Figure 9 shows the results for the unstable case [the LSA result is shown in Fig. 4(a)], where we take the domain size equal to the wavelength of maximum growth, i.e., $X=\lambda_m=2.66$. In agreement with the LSA, we see that the flow is unstable, with the long time evolution leading to the formation of two half drops, which represent a single drop within the wavelength λ_m. Therefore, this infinite flat film evolves to a steady-state configuration with drops separated by a distance $D=\lambda_m$.

Figure 9(b) shows the time evolution of the amplitude $\delta(t)$, defined as

$$\delta(t)=h_0-h(X/2,t). \tag{16}$$

We observe a very good agreement between the numerical solution and the LSA result, which predicts $\delta(t)=\epsilon\exp(\beta_m t)$ with $\beta_m=0.03105$. We note that the asymptotic value $\delta(t\to\infty)$ is slightly different from h_0-h_*; this difference is explained in Appendix B.

Figure 10 shows the response of the film in a much larger computational domain, $X=60$, initially perturbed by a number of wavelengths $\lambda_i=2X/i$ $(i=1,\ldots,50)$ in the form

$$h_0(x,0)=h_0\left(1+\epsilon\sum_{i=1}^{50}A_i\cos(2\pi x/\lambda_i)\right),$$

where the amplitudes A_i are chosen randomly in the range $[-1,1]$. The resulting steady pattern is formed by drops separated by an average distance $\bar{D}\approx 2.71$, which is very close to λ_m. We will discuss this result further in the context of finite films in Sec. IV.

As an example of a stable film, we consider $(h_*,h_0)=(0.07,0.1)$, and take $\lambda=7$ for which the LSA predicts $\beta=-5.48\times10^{-3}$. Figure 11(a) shows consistently that the free surface, specified by Eq. (15) at $t=0$, recovers the flat profile as $t\to\infty$. Figure 11(b) confirms that the time evolution of the amplitude $\delta(t)$ is in very good agreement with the growth rate predicted by the LSA.

We proceed now by considering the action of finite disturbances. Therefore, we consider a localized disturbance at $x=x_0$ of the form[26]

$$h(x,0)=h_0\{1-d\exp[-(x-x_0)^2/\ell^2]\}, \tag{17}$$

where d controls the maximum amplitude of the perturbation, and ℓ measures its width (we use $d=0.2$ and $\ell=0.2\lambda_m$).

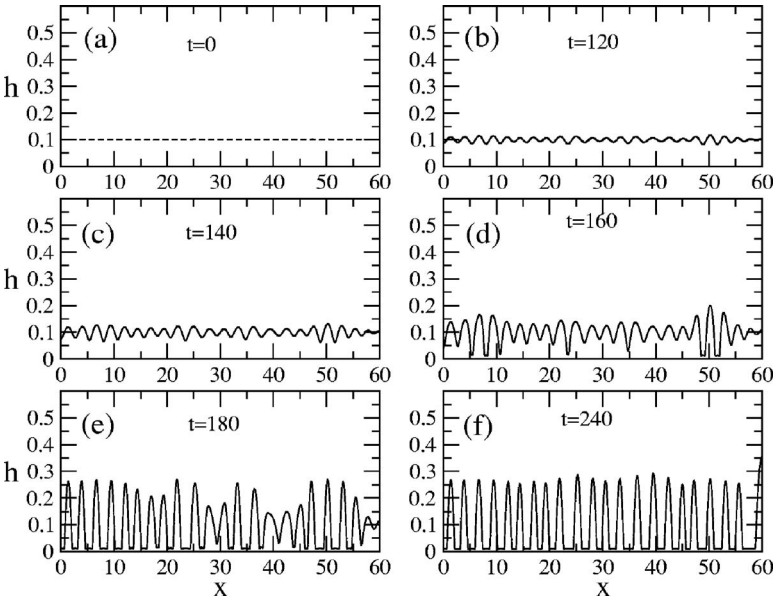

FIG. 10. Evolution of an unstable infinite film for $h_0=0.1$ and $h_*=0.01$, perturbed by a set of random perturbations. The last configuration shown ($t=240$) is steady on the considered time scales.

Within the linearly unstable region, we find, in agreement with the analysis carried out for the diffuse interface potential,[26,27] two regimes: surface instability dominated and nucleation instability dominated. Figure 12 shows a typical case of the evolution in the surface instability dominated regime ($h_0=0.05$): it evolves by forming a deep hole, and then traveling perturbations (in the form of undulations) emerge. Consequently, a finite-amplitude wave packet of increasing intensity expands in both directions, thus leading to a sequence of equispaced droplets. In this regime, the drops are separated by a distance very close to λ_m.

Figure 13 shows an example of nucleation dominated instability ($h_0=0.1$). It also evolves by initially forming a deep hole with rims at both sides, but here, as the hole expands, the depressions behind the rims eventually lead to another nucleation event, and then the process repeats again. In general, the distance between consecutive drops is different from λ_m, and in this case it is approximately $2\lambda_m$. We discuss later in the context of finite films other differences between the two regimes.

In the metastable region, as expected, the amplitude of the imposed localized perturbation must exceed a certain threshold in order to achieve a breakup. Our simulations show that for a large enough perturbation, the film breaks up and develops two diverging dewetting fronts. The film thickness at the fronts grows monotonically as they move apart without film breakup behind them. Of course, if multiple finite-size perturbations (nucleation centers) are present, multiple drops will form.[17–19] We note that future work is needed to find out whether the boundary between metastable and unstable regime is exactly the boundary relevant to film breakup via secondary nucleation or the formation of "satellite holes."[15,17,33]

Remark 1. Our numerical simulations do not find a well defined boundary between surface instability dominated and nucleation dominated regimes within the linearly unstable region of the parameter space. Instead, we find that there exists a "mixed" region so that for h_0 near the upper boundary line of the linearly unstable regime (see Fig. 8), the instability is mostly of nucleation type, while closer to the

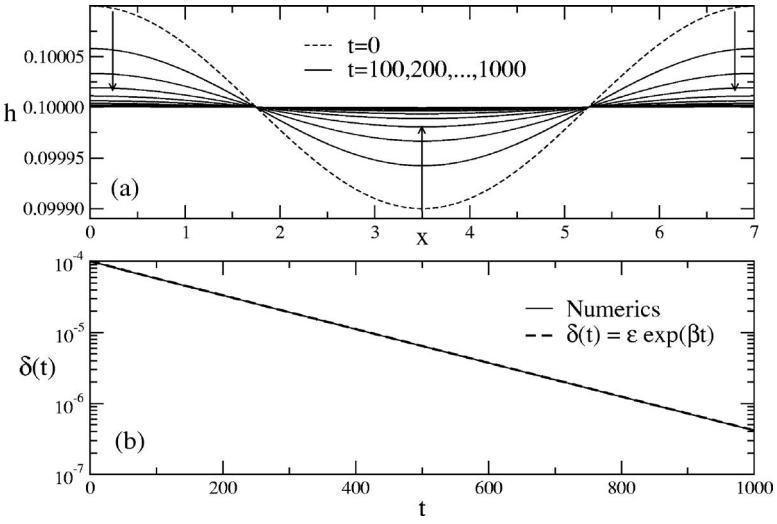

FIG. 11. Evolution of a *stable* infinite film for $h_0=0.1$ and $h_*=0.07$.

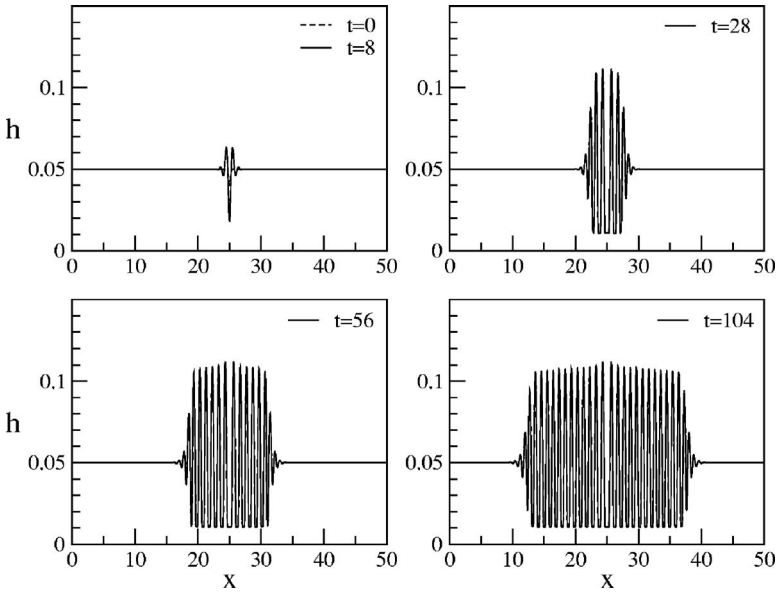

FIG. 12. Time evolution of a localized perturbation on an infinite film for $h_0=0.05$ and $h_*=0.01$, for which the LSA gives $\lambda_m=0.99$ (surface instability dominated regime).

lower boundary, surface instability is dominant.

Remark 2. Note that the response of an infinite linearly unstable film to infinitesimal and to finite-size perturbations in the nucleation dominated regime is significantly different. When perturbed by a number of modes of infinitesimal amplitude, the film chooses the wavelengths centered around λ_m from the LSA (viz., Fig. 10). However, a finite-size perturbation leads to a much larger average distance between the drops. We will find this result important when considering finite films in Sec. IV.

IV. FILM OF FINITE LENGTH

In this section, we consider a uniform film of finite length, L. To carry out a numerical study, we define a smooth initial profile as

$$h(x,0) = (h_0 - h_*)\{\arctan[q(x-x_1)] - \arctan[q(x-x_2)]\}/\pi + h_*, \tag{18}$$

where x_1 and x_2 are the coordinates of the end points of the bulk, so that the fluid length is $L=x_2-x_1$. The computational domain is $0\leqslant x\leqslant X=L+10$, and the fluid bulk is centered in this interval. The value of q determines the width of the transition region between the flat bulk of height $\approx h_0$ and the regions ($0<x<x_1$ and $x_2<x<X$) of thickness $\approx h_*$. We use a relatively large q (typically, $q=100$) to obtain an initial condition resembling a step function connecting h_0 and h_* at the end points of the bulk.

We note that, unlike in the infinite film case, the initial condition given by Eq. (18) does not correspond to an equilibrium configuration. Therefore, the flow evolves without any additional perturbation. First, we present the results for

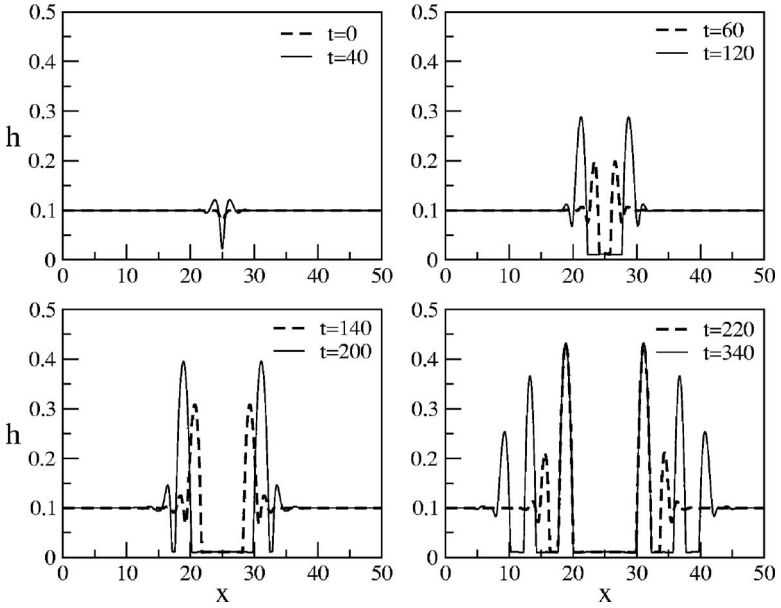

FIG. 13. Time evolution of a localized perturbation on an infinite film for $h_0=0.1$. Here, the LSA gives $\lambda_m=2.66$ (nucleation dominated regime).

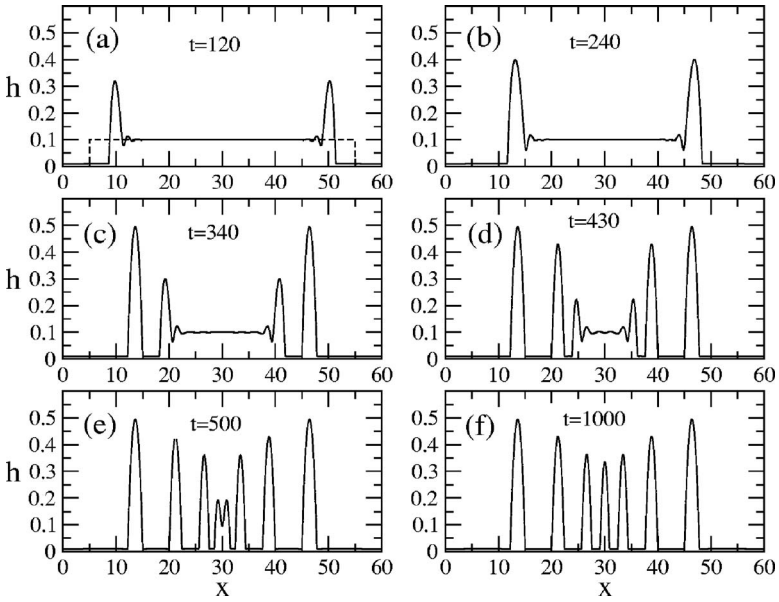

FIG. 14. Evolution of a finite fluid film of extension $L=50$ for $h_0=0.1$ and $h_*=0.01$.

this configuration, and then in Sec. IV B we consider also the presence of imposed surface perturbations. Thus, the cases shown in Sec. IV A analyze an ideal system, while those in Sec. IV B are closer to a physical one where surface perturbations are unavoidably present.

A. Evolution without surface perturbations

We first analyze films of finite length characterized by the values (h_*,h_0) within the linearly unstable region of the corresponding infinite film. Then, we consider the values (h_*,h_0) leading to metastable and stable infinite films.

1. Linearly unstable regime

Figure 14 shows a representative case of the evolution of a film whose initial condition is specified by Eq. (18). Behind each dewetting front, a ridge formed by the fluid volume swept by the front appears. The connection of the ridges to the remaining film is established via a damped oscillatory region, as also observed in experiments and simulations with nanometric polymer films.[17–19,63] As each front recedes, the minimum film thickness decreases until it reaches a value close to h_*, see Fig. 14(b), so that a virtual pinch-off occurs. This pinching process leads to the detachment of the receding ridges, which finally evolve into steady drops connected only by a thin film, see Fig. 14(c). The dewetting and pinching process continues until the whole bulk splits into a certain number of drops, see Figs. 14(d)–14(f).

Before proceeding to discuss the detail of the breakup process, we note that the mechanism described above is qualitatively similar to the experimental results presented in Fig. 1. In both cases, the instability propagates from the ends leading to an array of stationary drops. However, for a detailed comparison between theory and experiments, one needs to consider also the flow structure in the transverse direction (i.e., a rivulet in place of an infinite film). This problem is left for future work.

We note that even though the infinite film (Figs. 9 and 10) and the finite film (Fig. 14) share the same parameters, the resulting patterns are very different. For infinite films, the rupture process develops simultaneously everywhere, and the instability is triggered by small (imposed) perturbations driven by van der Waals forces (gravity as well as surface tension have stabilizing effects). Instead, for finite films, the receding fronts and the consequent formation of ridges introduce an additional mechanism of instability, without any imposed perturbations. Here, the rupture process does not occur simultaneously all along the bulk, but it proceeds from the ends toward the center.

Another important difference between finite and infinite films, which is particularly obvious if one compares Figs. 10 and 14, concerns the resulting wavelengths. While for infinite films one obtains wavelengths close to λ_m, for the finite film the resulting average distance between the drops is much larger, and close (in this example) to $2\lambda_m$. The fact that this average distance is similar to the one resulting from the response of an infinite film to a finite-amplitude perturbation (viz. Fig. 13) strongly suggests that an insight into the instability development of finite films can be reached by relating finite and infinite films. To discuss this idea more precisely, we consider next the emerging distance between the drops as the thickness, h_0, of (finite) films is varied.

Figure 15 shows the initial and final configurations for $L=50$, $h_*=0.01$, and h_0's in the range (0.05,0.15), corresponding to the linearly unstable interval for this value of h_*, see Fig. 8. We see that the number of drops strongly depends on h_0, with thicker films leading to a much smaller number of drops.

Table I shows the ratio of the distance, D, between the drops and λ_m for given h_0. We show the results both for $L=50$, presented in Fig. 15, and for $L=200$. The motivation for considering such a large domain is relatively large standard deviations of D for small L's, in particular if the resulting number of drops is small. We show only the results for $h_0<0.11$, where there is still a sufficient number of drops, in order to be able to estimate accurately the average distance.

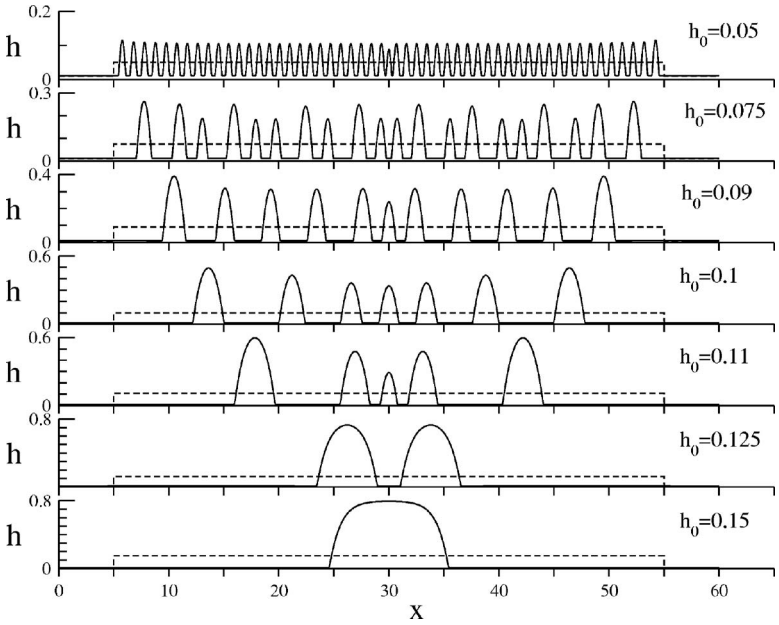

FIG. 15. Initial and final states of the evolution of a fluid bulk for different fluid thicknesses h_0. Here, $L=50$ and $h_*=0.01$.

The results in Table I clearly show that as h_0 is increased, there is also a gradual increase of D/λ_m. For thin films, this ratio is approximately unity, suggesting that the surface instability mechanism is relevant, similarly to the response of an infinite film to a finite-size perturbation, shown in Fig. 12. For large h_0, one obtains the values of D/λ_m that are characteristic of the nucleation dominated regime, resembling the evolution of infinite film shown in Fig. 13. For intermediate values of h_0 (e.g., $h_0=0.075$, viz. Fig. 15), one sees a transition between these two regimes.

Figure 16 illustrates this transition by presenting the discrete Fourier spectra of the thickness profiles. This figure shows that in the surface dominated regime there is a well defined peak in the Fourier spectrum very close to λ_m (dashed vertical lines). This peak is absent for the thicker films, in the nucleation dominated regime.

To conclude, we find strong evidence that instability of fluid films of finite extent can be explained by considering the response of an infinite film to finite-amplitude perturbations. The end effects act, at least to some degree, as finite-amplitude perturbations.

Remark 1. Recent experiments carried out with nanometric films[18] consider film evolution after the formation of a hole in a flat film. These experiments consider the radii of the holes at which film breakup (and so-called "satellite holes") occurs. It is found that these radii increase with film thickness. Although the emerging length scales (distance between drops, or rings in 3D) were not related in Ref. 18 to the wavelength of maximum growth from LSA, this observation appears to be consistent and can be explained based on the results presented here.

Remark 2. Figure 17 shows that the thickness of the thin film connecting the central drops is constant and a bit larger than h_* (see Appendix B). In addition, the film at the sides of the external drops is not uniform, indicating that the pressure is not completely balanced in this region. However, on the time scales considered here (up to 10^4-10^5 in our units) we do not observe coarsening effects such as those discussed recently.[64,65]

Remark 3. We note that the size of the drops and the distance between them is often not uniform, with the drops at the extremes and in the very center of an unstable film being slightly different from the rest. Thus, we consider also the

TABLE I. Ratio of the distance between final drops, D, and λ_m (mean value and the standard deviation), for different fluid thickness h_0. The wavelength of maximum growth, λ_m, for a corresponding infinite film is also shown. The results are obtained for the initial film lengths of $L=50$ and 200.

h_0	λ_m	D/λ_m $(L=50)$	D/λ_m $(L=200)$
0.05	0.99	0.94±0.14	0.94±0.09
0.075	1.74	1.34±0.42	1.26±0.29
0.09	2.27	1.72±0.64	1.65±0.41
0.10	2.66	2.05±1.06	1.93±0.52
0.11	3.09	1.97±1.38	2.56±0.62

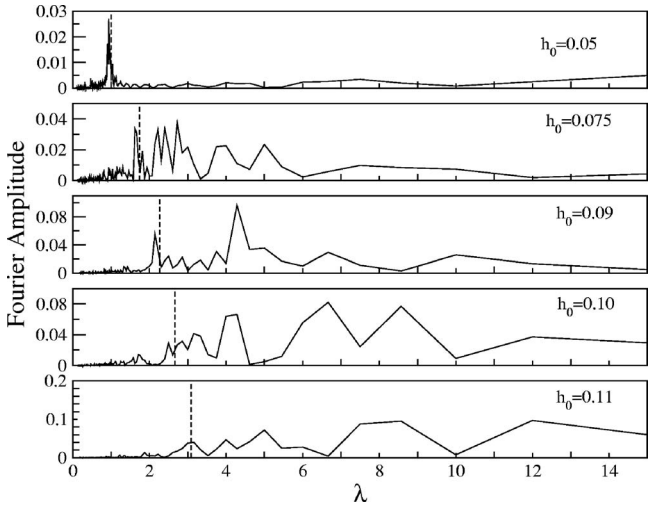

FIG. 16. Discrete Fourier transforms of the final states shown in Fig. 15. The vertical dashed lines indicate the corresponding values of λ_m.

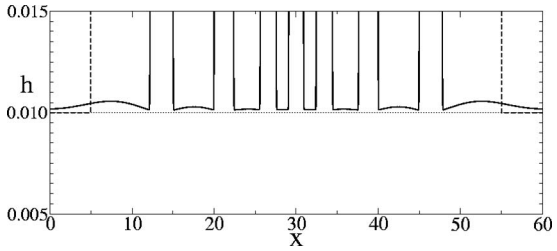

FIG. 17. Close up of the film region connecting the drops in the pattern of Fig. 14(f). The dashed and solid lines correspond to $t=0$ and 1000, respectively.

individual values of D_i as well as those of the drops widths, w_i, where the index i counts the drops starting from the center. Figure 18 shows these quantities. We observe that for $h_0=0.05$, the instability mechanism yields an array of many quasi-equidistant and almost identical droplets, while for $h_0=0.075$, the parameters $(w_i/\lambda_m, D_i/\lambda_m)$ alternate between two values. For larger h_0, both w_i and D_i increase monotonically with i.

2. Metastable and stable regimes

Figure 19 shows the evolution of a finite film inside the metastable region (and very close to the boundary of the linearly unstable region) for $(h_*, h_0)=(0.01, 0.2)$ and $L=50$. Similarly to the configurations considered in the preceding section, the film evolves by forming receding ridges behind the dewetting fronts. However, no breakup occurs behind the ridges. Thus, the evolution leads to the development of a single central drop after the coalescence of both ridges in the middle of a finite film. Additional simulations show that a single drop forms independently of the film length. These results suggest that the amplitudes of the perturbations on the flat region of the film due to the damped oscillations behind the ridges are not strong enough to destabilize uniform film, at least for the cases considered here.

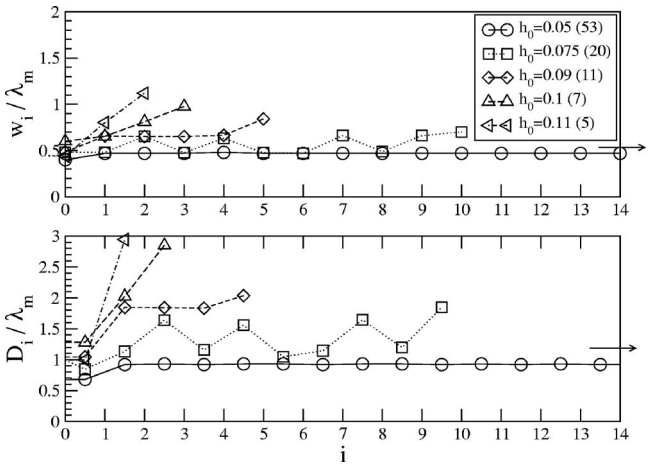

FIG. 18. The drop width, w_i, and the distance between the drops, D_i, in terms of λ_m for the ith drop and different fluid thicknesses, h_0. Here, $L=50$ and $h_*=0.01$. Only the right half of the drop pattern is considered ($i=0$ corresponds to the central drop), and the total number of drops, N, is indicated between parentheses. The arrow indicates additional drops for $h_0=0.05$.

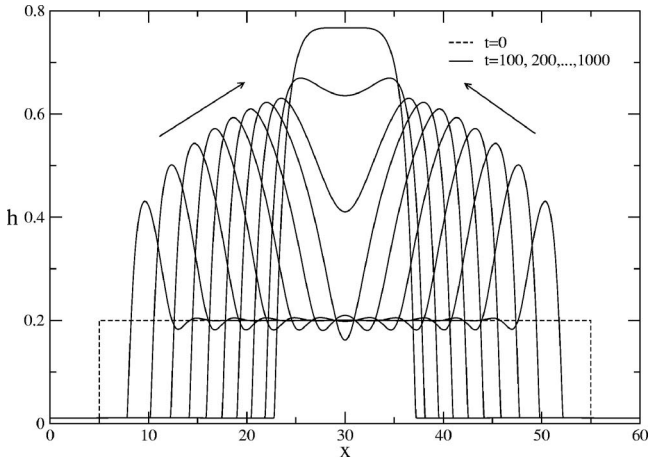

FIG. 19. Thickness profile evolution for $h_0=0.2$, $h_*=0.01$, and $L=50$. This case falls in the metastable region of Fig. 8.

In the stable region, the numerical results have basically the same features as in Fig. 19, i.e., they show a single central drop for any value of L. Therefore, in both regions, stable and metastable, the final single drop contains the total mass of the fluid. The drop width increases for larger L's, but the maximum height is bounded by $h_{0,\max}=\tan\theta$, as discussed in Appendix B. Thus, for very large L the central drop is basically a pancake, whose width and height are such that the drop is in equilibrium. The addition of imposed surface perturbations, which we consider in the following section, does not play any role in these regimes, since they fade out during the evolution.

3. Parametric dependence

Film length. Figure 20 shows the resulting drops for a wide range of film lengths. We see that if L is sufficiently small, very few or just a single drop result. For sufficiently large L, the average distance between the drops saturates to a value that is L-independent. This is illustrated further in Fig. 21, which shows the average area of a drop, $\bar{A}$, the number of drops, N, and the average distance between the drops, $\bar{D}$. We see that for large L, $\bar{A}$ and $\bar{D}$ tend to constant values, while N increases linearly with L.

Disjoining pressure: Equilibrium thickness h_*. So far, we have considered a fixed value of the van der Waals equilibrium thickness, $h_*=0.01$. As expected from the stability analysis of the infinite film, summarized in the stability diagram shown in Fig. 8, variations of h_* lead to significant changes in the evolution of a finite film. Figure 22 shows this effect: smaller h_* (while keeping h_0 fixed) brings us close to the boundary of the metastable regime and strongly decreases the number of resulting drops. Larger values of h_* result in a much larger number of drops, as also illustrated in this figure.

Disjoining pressure: The exponents n and m. Figure 23 shows the effect of varying the exponents (n, m) entering the disjoining pressure model. For the considered case, the evolution of the finite length film leads to an array of droplets only for (3,2), while a single drop results for both (4,3) and

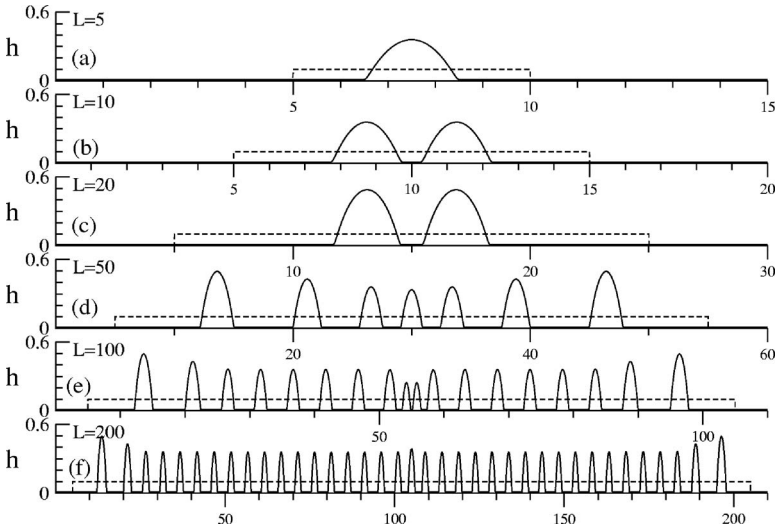

FIG. 20. Initial and final states of the evolution of a fluid bulk for different fluid extensions, L. Here, $h_0=0.1$ and $h_*=0.01$.

(9,3). We can explain this variation by recalling the linear stability diagram, Fig. 5. The configurations that fall deep inside the unstable region lead to breakup, and consequently to several drops, while the configurations that are close to the upper boundary with the stable region lead to a single drop.

Disjoining pressure: The contact angle. As expected, the variation of the contact angle (related to the parameters entering disjoining pressure model) also affects the final pattern. Figure 24 shows that an increase of θ yields a larger number of drops. We note that as θ increases, the considered (h_*,h_0) configuration falls deeper inside the unstable region (see Fig. 6). However, for small θ, the considered configuration is close enough to the upper boundary with the (meta)stable regime, so that it yields a single central drop. For even smaller θ's, the resulting drop is more extended and, consequently, lower. This is in agreement with the expectation that in the limit $\theta\rightarrow 0$ the fluid does not dewet the substrate but spreads out instead.

B. Finite film with surface perturbations in the nucleation dominated regime

In this section, we analyze the influence of externally imposed surface perturbations on the dewetting process of a finite film. We add sinusoidal perturbations of the film free surface in the form prescribed by Eq. (15), with h_0 replaced by $h(x,0)$ as given by Eq. (18). The perturbations are of wavelength, λ, that is close to λ_m, so that an integer number of λ's fits in a given film length. In this section, we concentrate on the nucleation dominated regime, since imposed perturbations in the surface dominated regime do not influence the dynamics significantly—that is, the resulting distances between the drops are almost the same with and without imposed perturbations.

Figure 25 shows the effect that surface perturbations have on the configurations previously considered in Fig. 20, which illustrated the influence of the fluid length on drop formation in the nucleation dominated regime. First we note that for small L (<20 or so), the results shown in these two

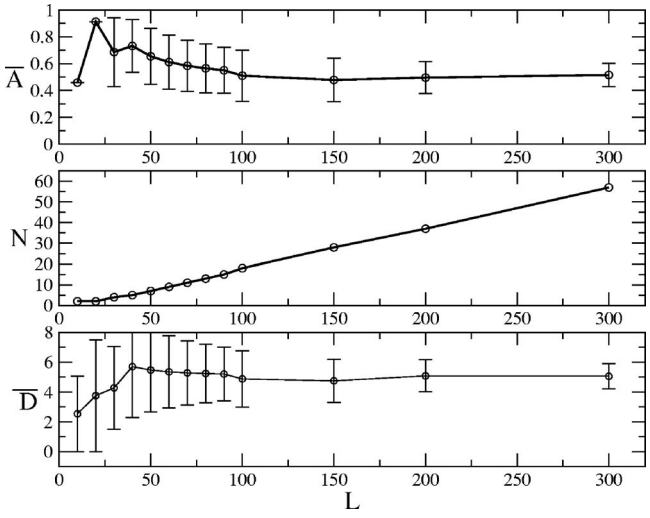

FIG. 21. Effects of the fluid length, L: (a) Average drop area, (b) number of final drops, (c) average distance between drop apexes. The error bars correspond to the standard deviations. Here, $h_0=0.1$ and $h_*=0.01$.

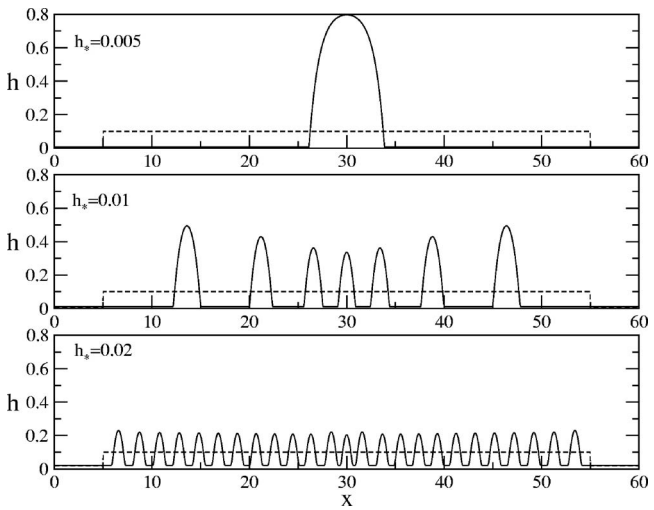

FIG. 22. Initial and final states of the evolution of a fluid bulk for different equilibrium thicknesses, h_*. Here, $L=50$ and $h_0=0.1$.

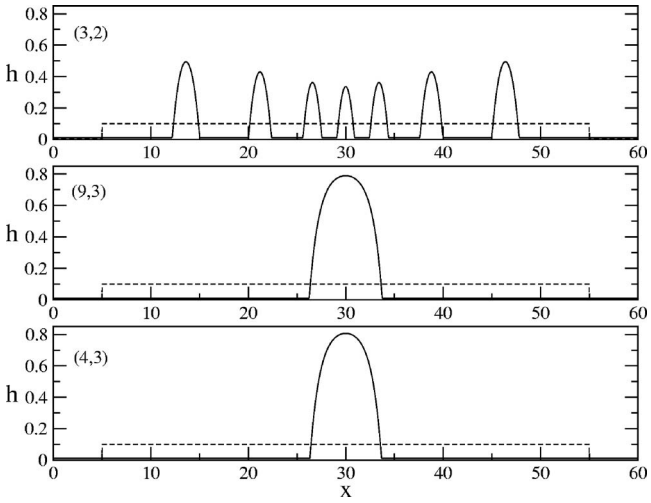

FIG. 23. Initial and final states of the evolution of a fluid bulk for different pairs (n,m). Here, $h_0=0.1$, $h_*=0.01$, and $L=50$.

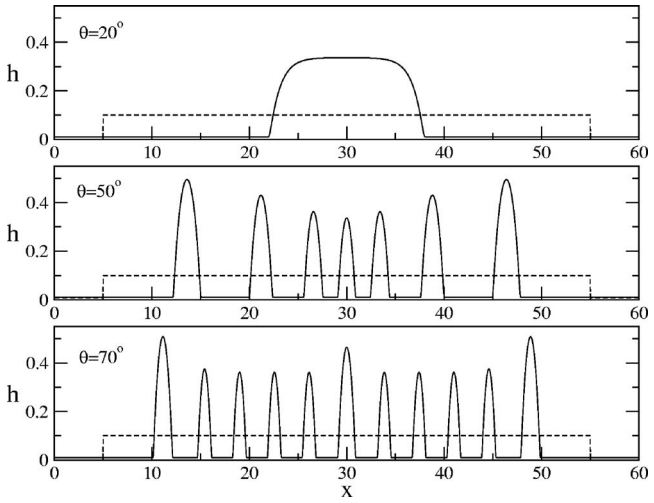

FIG. 24. Initial and final states of the evolution of a fluid bulk for different contact angles, θ. Here, $L=50$, $h_0=0.1$, and $h_*=0.01$.

figures are coincident. A natural explanation (which we quantify below) is that for $L<20$, the unstable mode of wavelength λ has no time to grow before the dewetting fronts meet at the center. For larger L's, the perturbation is able to grow, with the consequence that the number of drops, N, as well as their average distance, $\bar{D}$, strongly differ from the unperturbed case. Figure 26 illustrates the time evolution of the instability for $L=50$. The comparison with Fig. 15 shows that N increases from 7 to 15 and $\bar{D}$ decreases from 5.46 to 2.55 ($\approx\lambda_m$) due to the presence of surface perturbations.

Another significant influence of imposed perturbations is that since the internal drops start to form almost immediately after the beginning of the evolution, the time needed for the flow to reach the final configuration is much shorter, compared to the unperturbed case. The reduction can be as large as an order of magnitude for the imposed perturbations of initial amplitude of $10^{-3}h_0$.

In order to find the parameter region where surface instability prevails, we compare the time, τ_n, needed to dewet half the film length, with the time, τ_s, for a surface perturbation to grow enough to produce film breakup. Basically, we expect that if $\tau_s<\tau_n$, surface instability determines the main properties of the final pattern. Otherwise, nucleation instability is responsible.

To estimate τ_s, we assume that the LSA can be used even when a perturbation becomes large. Recalling that the initial amplitude of a perturbation is $\delta(t=0)=\epsilon h_0$, and since a breakup occurs when $\delta(\tau_s)\approx h_0$, the LSA for a perturbation of wavelength λ_m predicts

$$\tau_s=-\frac{\ln\epsilon}{\beta_m}. \tag{19}$$

An estimate of τ_n requires knowledge of the dewetting front dynamics. Although the issue of the speed of the dewetting front has been discussed in the literature,[16,15,66] results of general validity do not exist. For our purposes, we extract this information from the numerical results. Figure 27 shows the front position $x_f(t)$ for different combinations of h_0, h_*, and L. The data that form horizontal lines on this

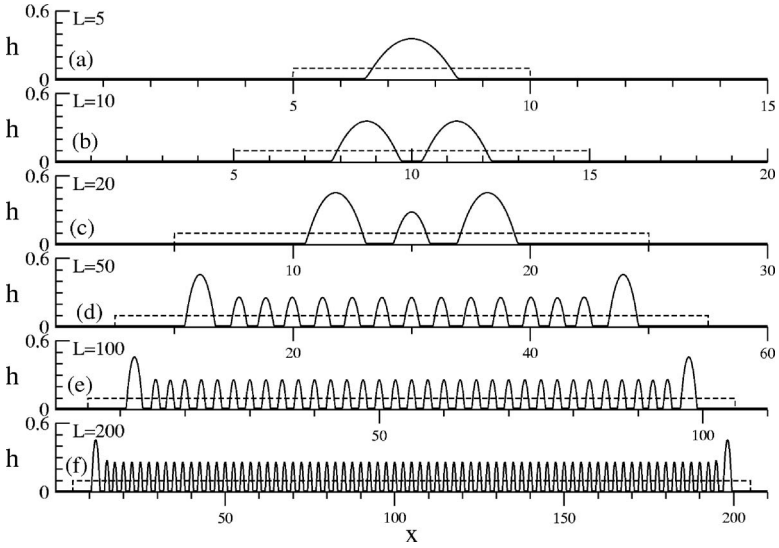

FIG. 25. Initial and final states of the evolution of the fluid films previously shown in Fig. 20, now with free surfaces perturbed at $t=0$ by $\lambda=2.5$.

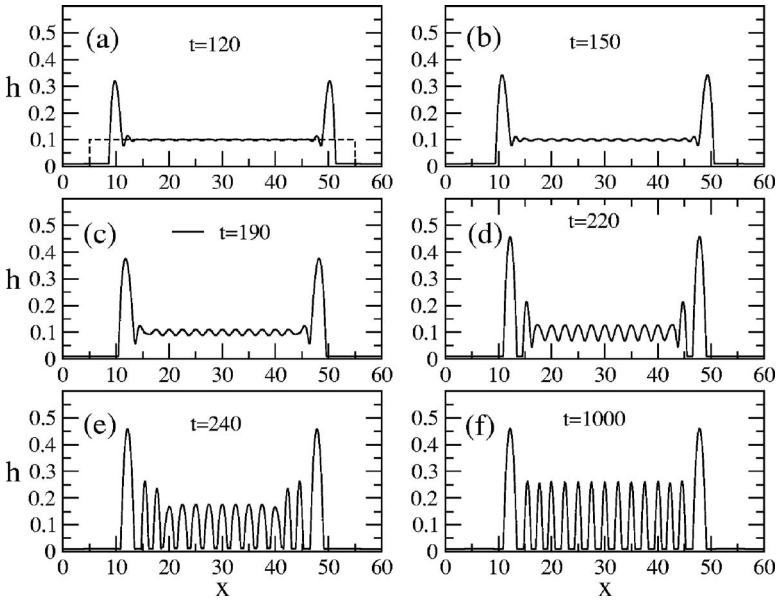

FIG. 26. Evolution of a finite fluid film of extension $L=50$ for $h_0=0.1$ and $h_*=0.01$. A sinusoidal perturbation of $\lambda=2.5$ is imposed on the film free surface.

figure correspond to the breakup of the film behind the ridges due to nucleation instability and the consequent stopping of that particular front. Behind the detached drop, a new front forms, whose velocity is similar to that of the preceding front. However, this new front starts propagating inward a certain distance ahead of the stopping point of the preceding front. This distance is approximately the width, w, of the drop that was formed. Thus, the effective distance traveled by the dewetting front is $\approx(L-N\bar{w})/2$.

For the time period shown in Fig. 27, we find that $x_f(t)$ is independent of L (circles and crosses), basically insensitive to the equilibrium thickness h_* (crosses and stars), and that an increase of h_0 only leads to a delay in reaching a long-time behavior (triangles and crosses). For the late times, all the results collapse onto a single curve (solid line in Fig. 27), which can be fitted by

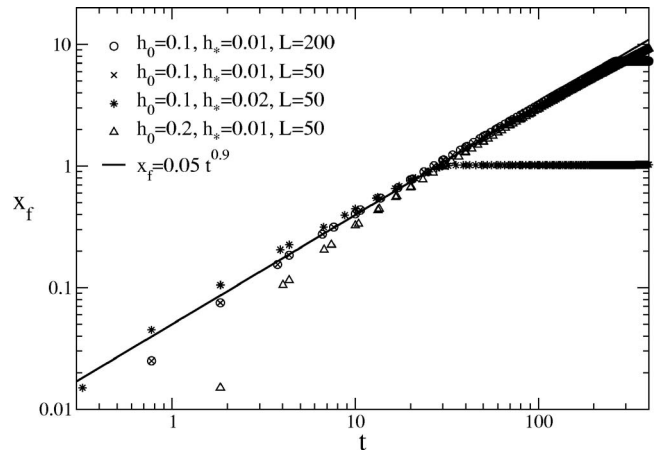

FIG. 27. Position of one of the dewetting fronts, $x_f(t)$, with respect to its initial position for several values of h_0, h_*, and L. Note that crosses and circles, which differ only in the value of L, are coincident.

$$x_f(t) = \xi_f t^{\alpha},$$

with $\xi_f \approx 0.05$ and $\alpha \approx 0.9$. By using this formula to estimate τ_n, we obtain

$$\tau_n = \left(\frac{L - N\bar{w}}{2\xi_f} \right)^{1/\alpha}. \tag{20}$$

Figure 28 shows the resulting τ_n (horizontal lines on this figure) and τ_s, following from Eq. (19). We see that for $h_0=0.1$ and $\epsilon=10^{-3}$, corresponding to the results shown in Fig. 25, the surface perturbations have time to grow before the side dewetting fronts coalesce at the middle of the film, provided that $L>L_{\mathrm{cr}}\approx 20$. Therefore, this result quantifies our earlier conjecture that the patterns obtained for larger values of L in Fig. 25 are due to the growth of surface perturbations.

Remark. Let us consider the results obtained for very small values of ϵ, also shown in Fig. 28. Since τ_s increases for smaller ϵ, the corresponding L_{cr} increases as well. We note that $\epsilon=10^{-16}$, which yields $L_{\mathrm{cr}}\approx 100$, is of the order of the double-precision roundoff error. Consistently, we may expect that simulations carried out *without* imposed surface perturbations, performed using double-precision arithmetic for $L>100$, may lead to growth of perturbations caused by this roundoff error. Figure 29 shows that this is indeed the case. For $L=200$, and *without* imposed perturbations, the flat central portion of the film destabilizes. As a result, the drop size and the distance between drops corresponds to the surface instability dominated regime, instead of to the nucleation dominated regime. For this reason, all simulations reported in this paper for $L>100$ were performed using quadruple precision arithmetic. Assuming that quadruple-precision corresponds to $\epsilon=10^{-32}$, from Fig. 28 we have $L_{\mathrm{cr}}\approx 200$. Therefore, any calculation beyond this length can

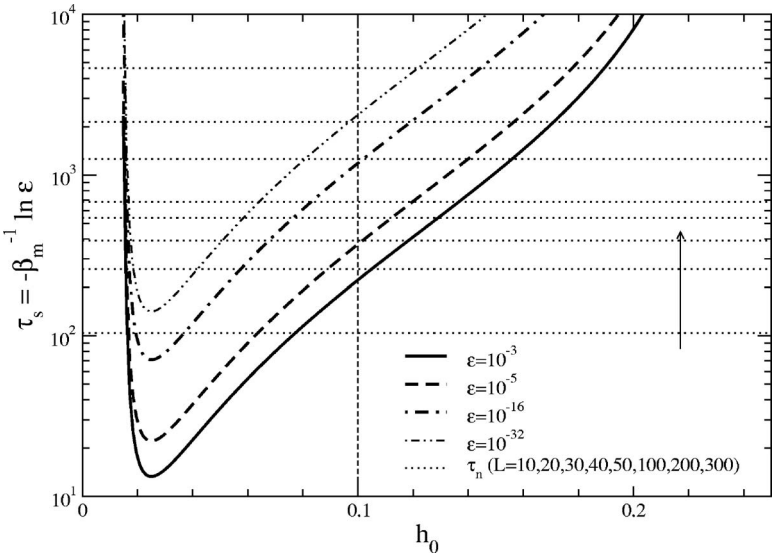

FIG. 28. Time τ_s necessary for a surface perturbation to grow up to breakup as a function of film thickness, h_0. The horizontal lines show the time to dewet half a film, τ_n, for various L's. The arrow shows the direction of increasing L (and τ_n). The vertical dashed line indicates $h_0=0.1$, a typical case considered here.

possibly lead to unreliable results. Of course, if additional perturbations are imposed in the (meta)stable regime, the growth of these spurious perturbations is not of concern.

V. SUMMARY AND CONCLUSIONS

We study the time evolution of a finite length film on a horizontal substrate under the action of surface tension, gravity, and van der Waals forces. Since the initial condition does not correspond to an equilibrium configuration, the film evolves by dewetting the surface. This receding motion of the fronts leads to the formation of ridges at the film ends, where the fluid thickness increases as more mass is swept inwards. Depending on the original film thickness, h_0, contact angle, θ, and the type of intermolecular van der Waals force, the film just behind the ridges may break up, thus producing a detached drop and a new dewetting front. This mechanism repeats itself until the whole film breaks up into a steady array of droplets.

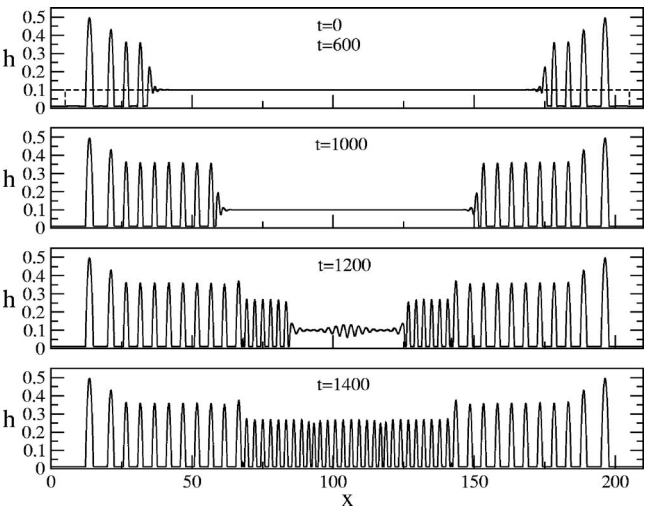

FIG. 29. Evolution of a finite fluid film *without* externally imposed surface perturbations under double-precision computer arithmetic, using $L=200$ for $h_0=0.1$ and $h_*=0.01$; viz. Fig. 25 for quadruple-precision results. Roundoff errors $O(10^{-16})$ introduce spurious surface perturbations for this relatively long film.

We base our analysis of the results on the stability properties of an infinite film. We find that the finite films whose infinite counterparts are stable or metastable do not break up, but instead collapse to a single central drop generated by the coalescence of the dewetting fronts. However, the finite films whose infinite counterparts are linearly unstable break up into a pattern of droplets. The average distance, $\bar{D}$, between these droplets does not, in general, correspond to the wavelength of maximum growth, λ_m, resulting from the linear stability analysis of an infinite film. Only for relatively thin films (of thickness h_0) we find $\bar{D} \approx \lambda_m$. As h_0 increases, $\bar{D}$ increases as well relative to λ_m. For intermediate values of h_0, the distance between drops may oscillate, indicating the presence of a mixed regime. The resulting wavelengths for finite films are generally similar to the ones resulting from a finite-amplitude perturbation of a corresponding infinite film, therefore suggesting that the fronts could be considered as finite-amplitude perturbations.

The length of the film, L, plays a role in determining the final pattern. For L sufficiently small, the breakup behind the receding ridges does not take place, and their coalescence at the middle of the domain leads to a single central drop. For larger L's, an increasing number of droplets is generated in the successive breakups. For these L's, we find that very careful simulations including the use of quadrupole-precision computer arithmetic are needed, since numerical noise can lead to spurious instabilities.

In addition to understanding experiments performed on a microscale, we expect that the presented results will be useful for understanding experiments and simulations performed with nanometric films perturbed by finite-size perturbations. Similar effects observed in these systems suggest that analysis of finite films could help explain instability mechanisms for a wide range of problems.

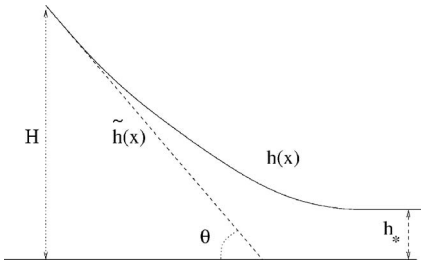

FIG. 30. Assumed shape of the free surface near the contact line.

APPENDIX A: PARTIAL WETTING WITH VAN DER WAALS FORCES

When a fluid partially wets the substrate, the thickness profile near the contact line can be represented mathematically by using the Frumkin-Deryaguin model.[67] Within this model, the substrate region near the fluid front is covered with a submicroscopic layer of liquid. This wetting layer (usually called precursor film) is maintained in a state of stable equilibrium through the action of intermolecular forces. In this frontal film, there is excess or "disjoining" pressure that is due to the fact that the intermolecular forces experienced by a volume element in the interior of the precursor film are different from those acting on an identical element in the interior of the bulk phase of the same fluid. These forces are customarily divided into long-range molecular, ionic-electrostatic, and structural components. The first group includes dispersion forces between pairs of nonpolar molecules, and also induction forces (mainly dipole-dipole interaction) when one of them is a polar molecule (see, e.g., Ref. 68 for a complete survey).

The length scale on which disjoining pressure is significant is typically less than the wavelength of visible light. Thus, even when the fluid wets the substrate, the meniscus at observable distances may appear to intersect the solid at a nonzero contact angle. The observed angle, whether by the naked eye or through the usual microscope, is called the apparent contact angle, θ.

The actual liquid-air interface $h(x)$ (solid line in Fig. 30) near the contact line satisfies

$$p = -\gamma c - \Pi(h) = \text{const}, \tag{A1}$$

where p is the total pressure, γ is the surface tension, Π is the disjoining pressure, and

$$c = -\frac{d}{dh}[(1+h_x^2)^{-1/2}]$$

is the curvature (for a quasi-2D problem, $c \approx h_{xx}$ for $h_x \ll 1$). The dashed line in Fig. 30 is the extrapolated profile $\tilde{h}(x)$ that results when the intermolecular forces at the contact line are ignored, i.e., when Π is set to zero,

$$p = -\gamma c(\tilde{h}) = \text{const}. \tag{A2}$$

Integrating Eq. (A1) from far away of the substrate, say $h=H \gg h_*$, to some equilibrium (to be discussed below) thickness h_*, and similarly integrating Eq. (A2) down to the solid surface ($\tilde{h}=0$), and then taking the limit $H \to \infty$, we obtain

$$\cos\theta = 1 - \frac{\lim_{H\to\infty}\sigma(h_*,H)}{\gamma}, \tag{A3}$$

with

$$\sigma(h_*,H) = -h_*\Pi(h_*) - \int_{h_*}^{H}\Pi(h)dh, \tag{A4}$$

where we have replaced $p=-\Pi(h_*)$ from Eq. (A1), and used $\tilde{h}_x(H)=h_x(H)$ and $c(h_*)=0$. This is the disjoining-model equivalent of the Young-Laplace equation, sometimes referred to as the "augmented" equation. Recalling the definition of the spreading coefficient

$$\cos\theta = 1 - \frac{S}{\gamma},$$

we note the simple connection between $\sigma(h_*,H)$ and $S=\gamma+\gamma_{SL}-\gamma_{SV}$, where γ_{SL} and γ_{SV} denote the solid-liquid and solid-vapor interfacial energies, respectively.

If $\sigma(h_*,H)<0$ (and correspondingly $S<0$), only complete wetting is possible, and $\theta=0$. In particular, this occurs when $\Pi(h)>0$ for all h. In contrast, we have partial wetting if $\Pi(h)<0$ for some h, since $\sigma(h_*,H)$ may become positive. Here, h_* is defined as the equilibrium thickness when the fluid is under the action of intermolecular forces only, and so $\Pi(h_*)=0$ and, consequently, $p=0$ for $h=h_*$. The value of h_* depends on the particular form of $\Pi(h)$, and it is a characteristic of the molecular interaction between the liquid, solid, and vapor.

Several forms for the disjoining pressure, $\Pi(h)$, can be found in the literature.[54] Here, we use a general expression for the apolar van der Waals intermolecular solid-liquid interactions in the form

$$\Pi(h) = \kappa f(h) = \kappa\left[\left(\frac{h_*}{h}\right)^n - \left(\frac{h_*}{h}\right)^m\right], \tag{A5}$$

where κ (proportional to the Hamaker constant) and the exponents n and m are positive constants with $n>m>1$. The first term represents liquid-solid repulsion, while the second term is attractive, leading to a stable film thickness $h=h_*$; thus, $\Pi>0$ if $h<h_*$ and $\Pi<0$ otherwise. We note that more complex models for disjoining pressure are available.[58–61] For the model considered here, the stability of the thickness $h=h_*$ is clear if one considers the stored energy per unit area,

$$\Omega(h) = -\int_{h_*}^{h}\Pi(h)dh = \kappa[u(h)-u(h_*)],$$

where $u(h)$ is given by Eq. (13). Recalling that $\Omega(\infty)=S$, the constant κ is given by

$$\kappa = S/(Mh_*),$$

with $M=(n-m)/[(m-1)(n-1)]$. Thus, we can write

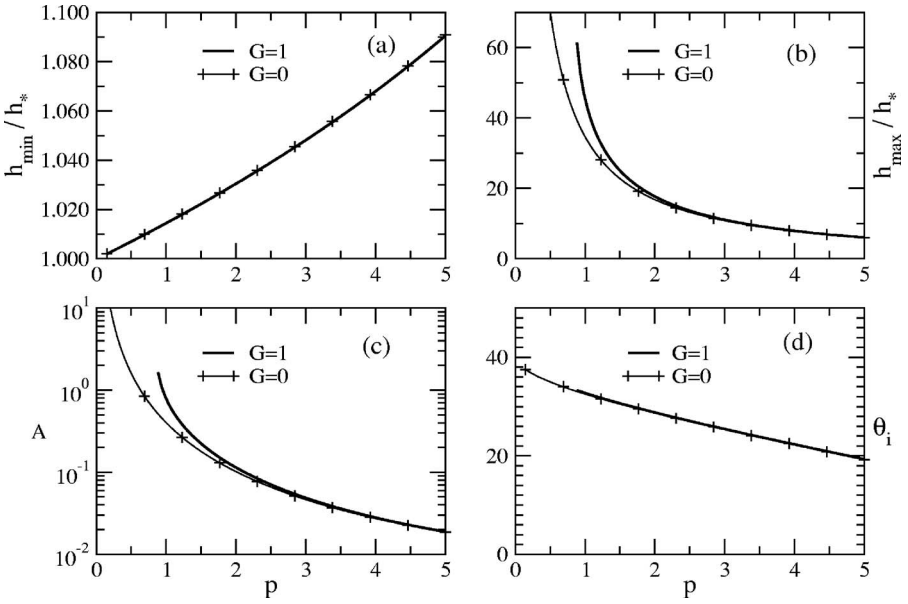

FIG. 31. Sessile drop properties as a function of equilibrium pressure p for $n=3$, $m=2$, $\theta=50°$, and $h_*=0.01$: (a) thickness of the film far away from the drop, (b) thickness at the center of the drop, (c) drop area, (d) angle at the inflection point, θ_i ($G=1$, black thick lines; $G=0$, thin lines with crosses).

$$\Omega(h) = \kappa u(h) + S. \tag{A6}$$

As a consequence, the prefactor for the disjoining pressure, κ, is determined by the value of the macroscopic contact angle, θ, the equilibrium thickness, h_*, and a pair of exponents, (n,m), which characterizes the solid-liquid interaction. The pair (3,2) is suggested in Ref. 55, while the pair (9,3) results from volume integration of molecular forces arising from Lennard-Jones 6–12 potential.[56]

We note that the disjoining pressure formulation naturally introduces a precursor film, whose thickness is close to h_*. In Appendix B, we discuss, among other issues, the relation of the actual precursor film to the van der Waals equilibrium thickness, h_*, arising from the fact that H used above needs to be given a large (but finite) value.

APPENDIX B: SINGLE DROP SOLUTION

Since the final pattern after breakup of both finite and infinite films consists of an array of drops at rest, here we study the steady-state solution of Eq. (4) corresponding to a steady single drop. The main result is that the length of a single drop increases as its mass is increased, but its thickness is bounded by a maximum value as discussed in Sec. IV (see also Ref. 69). This result is independent of the intermolecular potential, and it is a direct consequence of the balance between gravity and surface tension forces. Only the exact value of this maximum thickness depends on the intermolecular potential considered in the calculation. To show this, we will discuss the solutions with and without gravity, and with and without van der Waals forces.

After setting $\partial h/\partial t=0$ in Eq. (4), the resulting equation is integrated twice. By using the boundary conditions $h'''=h'=0$ at $x=\pm\infty$, where the primes stand for x derivatives, we obtain

$$h'' + Kf(h) - Gh + p = 0, \tag{B1}$$

where the constant p is the equilibrium pressure.[64,70] Note that for $h>h_*$, both the curvature h'' and disjoining pressure $Kf(h)$ are negative, so that $p>0$.

At infinity, where $h''=0$, the film has a minimum thickness, h_{min} (precursor film thickness). It is of the order of h_* and satisfies

$$Kf(h_{min}) - Gh_{min} + p = 0. \tag{B2}$$

An insight regarding the value of h_{min} can be reached by considering $G=0$ and expanding $f(h)$ [see Eq. (A5)] around h_*,

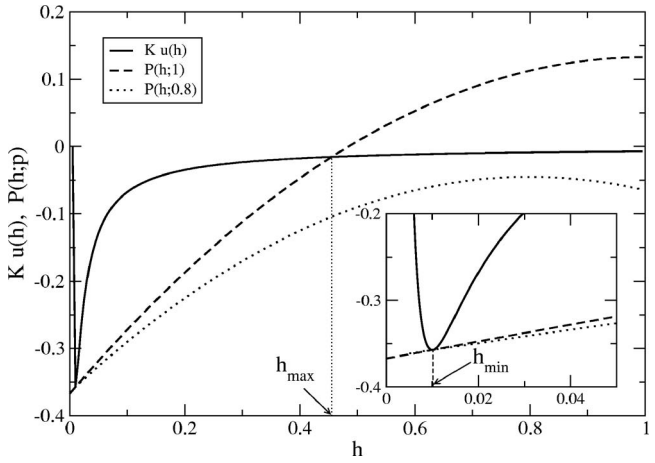

FIG. 32. Plot of the left-hand side and right-hand side of Eq. (B4). The inset shows a blowup of the region close to h_{min}.

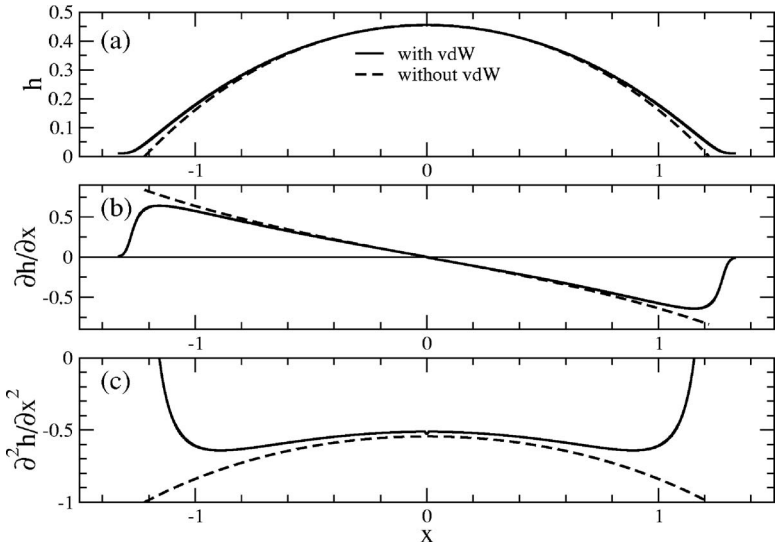

FIG. 33. (a) Profile of thickness $h(x)$, (b) slope $h'(x)$, and (c) curvature $h''(x)$ for $p=1$ with van der Waals forces included (solid lines) and excluded (dashed lines) (n, m, h_*, and θ are as in Fig. 31).

$$h_{\min} \approx h_* + \frac{ph_*}{K(n-m)}.$$

Since $p>0$, $h_{\min}$ is always greater than h_*, i.e., the actual precursor film is thicker than the equilibrium film resulting from van der Waals forces.

Figure 31 presents a number of single drop results, and it is central to this appendix. Figure 31(a), which shows the numerical solution of Eq. (B2), illustrates that $h_{\min}$ essentially does not depend on G, and that $h_{\min} \to h_*$ as $p \to 0$. For the considered values of θ, n, and m, the difference between h_* and $h_{\min}$ is at most few percent.

Next we discuss the maximum thickness of the drop, $h_{\max}$. Upon integrating Eq. (B1), we have

$$h'^2/2 - Ku(h) - Gh^2/2 = -ph + C, \tag{B3}$$

where $u(h)$ is given by Eq. (13) and

$$C = -Ku(h_{\min}) - Gh_{\min}^2/2 + ph_{\min}.$$

At the center of the drop, $h=h_{\max}$ and $h'=0$, so that $h_{\max}$ is a solution of

$$Ku(h) = -Gh^2/2 + ph - C. \tag{B4}$$

Thus, $h_{\max}$ is given by the intersection of the curve $Ku(h)$ and the parabola $P(h;p)=-Gh^2/2+ph-C$. Figure 32 shows these curves for two values of p [it is easy to verify that these curves are tangent at $h_{\min}$, see Eqs. (B2) and (13)]. For $G=1$, we find that, for sufficiently small ($p<p_c \approx 0.84517$ for our choice of parameters), the only contact between these curves occurs at $h_{\min}$. For $G=0$, $P(h;p)$ reduces to a straight line, and it always intersects $Ku(h)$. Then, there is no such lower bound of p. The physical interpretation of this result is discussed below.

The drop profile itself can be written implicitly as [see Eq. (B3)]

$$x(h) = \int_h^{h_{\max}} \frac{dh}{\sqrt{R(h)}},$$

where

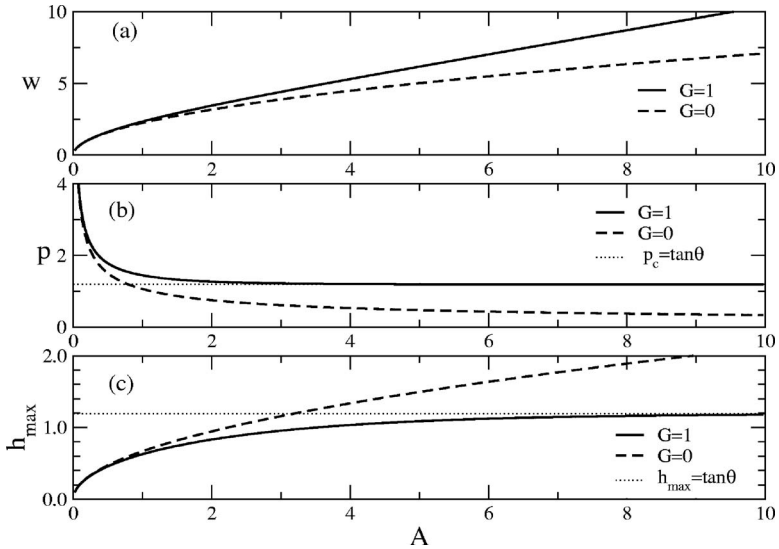

FIG. 34. (a) Drop width, w, (b) equilibrium pressure, p, and (c) thickness at the apex, $h_{\max}$, for the bulk solution (without van der Waals forces) as a function of the drop area, A, for $\theta=50°$.

$$R(h) = h'^2 = 2Ku(h) + Gh^2 + 2(-ph + C).$$

Figure 33 shows $h(x)$ and its derivatives (solid lines) for the parameters as in Fig. 31 with $p=1$. As expected, the thickness profile in Fig. 33(a) resembles that of a cylindrical cap, with a linear slope [Fig. 33(b)] and constant curvature [Fig. 33(c)]. At the drop edges, the slope smoothly goes to zero, the curvature reaches a maximum, and then decreases abruptly (not shown in the figure). We note that the slope at the inflection point, $\tan\theta_i$ [the maximum in Fig. 33(b)], is always less than $\tan\theta$ (following from the van der Waals model, discussed in Appendix A).

With $x(h)$ given, the area of the drop can be calculated as

$$A = 2\int_{h_{\min}}^{h_{\max}} x(h)dh.$$

Figure 31(c) shows A versus p for $G=0$ and 1. With gravity effects excluded ($G=0$), both A and $h_{\max}$ increase monotonically as p decreases. For $G=1$, similar behavior is found, except that A and $h_{\max}$ are not well defined for $p<p_c$. Consequently, for drops with area A larger than some critical value A_c, the pressure saturates at p_c independently of the drop size.

Figure 31(d) shows the actual contact angle of the solution, θ_i (the angle at the inflection point), as a function of p for $G=0$ and 1. As expected, gravity effects do not influence θ_i. We note in passing that θ_i is smaller than θ defined by the van der Waals model. This difference is another consequence of the fact that maximum drop thickness is bounded by $h_{\max}$.

We next consider the solution without van der Waals forces, since we expect that in the bulk region, sufficiently inside the drop, these forces are not relevant. If that is the case, the profile can be described by $h''-Gh+p=0$, with the boundary conditions $h=0$ and $|h'|=\pm\tan\theta$ at the drop edges $\mp x_f$. For $G=1$, this equation yields the analytical solution

$$h_{b1}(x) = p\left(1 + \frac{\sinh(x-w/2) - \sinh(x+w/2)}{\sinh w}\right), \tag{B5}$$

where $w=2x_f$ is the width of the drop, given implicitly by

$$A = 2\tan\theta\left(\frac{w/2}{\tanh(w/2)} - 1\right), \tag{B6}$$

and the equilibrium pressure $p(w)$ is obtained as

$$p = \frac{\tan\theta}{\tanh(w/2)}. \tag{B7}$$

Figure 33 shows a comparison between h_{b1} and the solution that includes van der Waals forces. The main differences are in the contact regions where the slope and curvature are significantly affected.

Finally, the thickness at the apex is calculated from p and w as

$$h_{\max} = p\left(1 - \frac{2\sinh(w/2)}{\sinh w}\right).$$

The quantities w, p, and $h_{\max}$ are plotted in Fig. 34 as a function of A for $\theta=50°$. We note that while w increases monotonically with A, both p and $h_{\max}$ asymptote to the value $\tan\theta$, since Eqs. (B6) and (B7) can be rewritten as

$$w = 2\arg\tanh\left(\frac{\tan\theta}{p}\right),$$

$$A = pw - 2\tan\theta.$$

Thus, we see that p is bounded from below, analogously to the result obtained when van der Waals forces are included. This result shows that the existence of both a minimum pressure and a maximum drop thickness is not a consequence of the intermolecular forces at the contact line, but it is an effect related only with the balance between gravitational and surface tension forces. The details of intermolecular interaction only influence the value of minimum pressure. Thus, we have $p_c \approx 0.84517$ for our van der Waals force, while $p_c=\tan\theta \approx 1.1917$ when no intermolecular force is taken into account and a contact angle θ is imposed at $h=0$.

For completeness, let us consider the bulk solution for $G=0$. In this case, the thickness profile is described by $h''+p=0$, so that the solution is

$$h_{b0} = \frac{p}{2}(x^2 - x_f^2), \quad 0 \leqslant x \leqslant x_f.$$

The area $A=2\int_0^{x_f} h(x)dx$ and the width w of the drop are given by

$$w = \frac{2\tan\theta}{p}, \quad A = \frac{pw^3}{12}.$$

Similarly to the case when van der Waals forces are included, no lower bound exists for p when gravity is not considered.

[1] K. J. Ruschak, "Coating flows," Annu. Rev. Fluid Mech. **17**, 65 (1999).
[2] H. S. Kheshgi, "The fate of thin liquid films after coating," in *Liquid Film Coating*, edited by S. F. Kistler and P. M. Scheizer (Chapman and Hall, London, 1997), p. 183.
[3] R. G. Larson and T. J. Regh, "Spin coating," in *Liquid Film Coating*, edited by S. F. Kistler and P. M. Scheizer (Chapman and Hall, London, 1997), p. 709.
[4] H. A. Stone, A. D. Stroock, and A. Ajdari, "Engineering flows in small devices," Annu. Rev. Fluid Mech. **36**, 381 (2004).
[5] H. A. Stone and S. Kim, "Microfluidics: Basic issues, applications and challenges," AIChE J. **47**, 1250 (2001).
[6] P. Weiss, "To bead or not to bead?" Sci. News (Washington, D. C.) **155**, 28 (1999).
[7] V. S. Mitlin, "Dewetting of solid surface: Analogy with spinodal decomposition," J. Colloid Interface Sci. **156**, 491 (1993).
[8] J. W. Cahn and J. E. Hilliard, "Free energy of a nonuniform system. 1: Interfacial free energy," J. Chem. Phys. **28**, 258 (1958).
[9] G. Reiter, "Dewetting of thin polymer films," Phys. Rev. Lett. **68**, 75 (1992).
[10] A. Sharma and R. Khanna, "Pattern formation in unstable thin liquid films," Phys. Rev. Lett. **81**, 3463 (1998).
[11] A. Sharma, "Instability and morphology of thin liquid films on chemically heterogeneous substrates," Phys. Rev. Lett. **84**, 931 (2000).
[12] K. Kargupta and A. Sharma, "Templating of thin films induced by dewetting on patterned surfaces," Phys. Rev. Lett. **86**, 4536 (2001).
[13] K. Neuffer and M. Bestehorn, "Surface patterns of laterally extended thin liquid films in three dimensions," Phys. Rev. Lett. **87**, 046101 (2001).
[14] K. Kargupta and A. Sharma, "Dewetting of thin films on period physically and chemically patterned surfaces," Langmuir **18**, 1893 (2002).
[15] K. Kargupta and A. Sharma, "Creation of ordered patterns by dewetting of thin films on homogeneous and heterogeneous substrates," J. Colloid Interface Sci. **245**, 99 (2002).
[16] A. Sharma, "Many paths to dewetting in thin films: Anatomy and physi-

ology of surface instability," Eur. Phys. J. E **12**, 397 (2003).
[17] J. Becker, G. Grün, R. Seemann, H. Mantz, K. Jacobs, K. R. Mecke, and R. Blossey, "Complex dewetting scenarios captured by thin-film models," Nat. Mater. **2**, 59 (2003).
[18] C. Neto, K. Jacobs, R. Seemann, R. Blossey, J. Becker, and G. Grün, "Satellite hole formation during dewetting: Experiment and simulation," J. Phys.: Condens. Matter **15**, 3355 (2003).
[19] C. Neto and K. Jacobs, "Dynamics of hole growth in dewetting polystyrene films," Physica A **339**, 66 (2004).
[20] A. Münch, "Dewetting rates of thin liquid films," J. Phys.: Condens. Matter **17**, S309 (2005).
[21] R. Seemann, S. Herminghaus, C. Neto, S. Schlagowski, D. Podzimek, R. Konrad, H. Mantz, and K. Jacobs, "Dynamics and structure formation in thin polymer melt films," J. Phys.: Condens. Matter **17**, S267 (2005).
[22] P. G. de Gennes, "Wetting: Statics and dynamics," Rev. Mod. Phys. **57**, 827 (1985).
[23] L. Leger and J. F. Joanny, "Liquid spreading," Rep. Prog. Phys. **155**, 28 (1999).
[24] L. M. Pismen and Y. Pomeau, "Disjoining potential and spreading of thin liquid layers in the diffuse-interface model coupled to hydrodynamics," Phys. Rev. E **62**, 2480 (2000).
[25] U. Thiele, M. G. Velarde, and K. Neuffer, "Dewetting: Film rupture by nucleation in the spinodal regime," Phys. Rev. Lett. **87**, 016104 (2001).
[26] U. Thiele, M. G. Velarde, K. Neuffer, and Y. Pomeau, "Film rupture in the diffuse interface model coupled to hydrodynamics," Phys. Rev. E **64**, 031602 (2001).
[27] U. Thiele, K. Neuffer, M. Bestehorn, Y. Pomeau, and M. G. Velarde, "Sliding drops on an inclined plane," Colloids Surf., A **206**, 87 (2002).
[28] U. Thiele, "Open questions and promising new fields in dewetting," Eur. Phys. J. E **12**, 409 (2003).
[29] R. Xie, A. Karim, J. F. Douglas, C. C. Han, and R. A. Weiss, "Spinodal dewetting of thin polymer films," Phys. Rev. Lett. **81**, 1251 (1998).
[30] K. Kargupta, R. Konnur, and A. Sharma, "Instability and pattern formation in thin liquid films on chemically heterogeneous substrates," Langmuir **16**, 10243 (2000).
[31] G. Reiter and A. Sharma, "Auto-optimization of dewetting rates by rim instabilities in slipping polymer films," Phys. Rev. Lett. **87**, 166103 (2001).
[32] A. Sharma and R. Verma, "Pattern formation and dewetting in thin films of liquids showing complete macroscale wetting: From pancakes to Swiss cheese," Langmuir **20**, 10337 (2004).
[33] S. Herminghaus, R. Seeman, and K. Jacobs, "Generic morphologies of viscoelastic dewetting fronts," Phys. Rev. Lett. **89**, 056101 (2002).
[34] H. Sirringhaus, T. Kawase, R. H. Friend, T. Shimoda, M. Inbaskearan, W. Wu, and E. P. Woo, "High-resolution inkjet printing of all-polymer transistor circuit," Science **290**, 2123 (2000).
[35] Y. Xia and G. M. Whitesides, "Soft lithography," Annu. Rev. Mater. Sci. **28**, 153 (1998).
[36] J. A. Rogers, "Towards paperlike displays," Science **291**, 1502 (2001).
[37] S. Schiaffino and A. A. Sonin, "Formation and stability of liquid and molten beads on a solid surface," J. Fluid Mech. **343**, 95 (1997).
[38] P. C. Duineveld, "The stability of ink-jet printing lines of liquid with zero receding contact angle on a homogeneous substrate," J. Fluid Mech. **477**, 175 (2003).
[39] A. G. González, J. Diez, R. Gratton, and J. Gomba, "Rupture of a fluid strip under partial wetting conditions," Europhys. Lett. **77**, 44001 (2007).
[40] B. J. Bentley and L. G. Leal, "An experimental investigation of drop deformation and breakup in steady, two-dimensional linear flows," J. Fluid Mech. **167**, 241 (1986).
[41] H. A. Stone, B. J. Bentley, and L. G. Leal, "An experimental study of transient effects in the breakup of viscous drops," J. Fluid Mech. **173**, 131 (1986).
[42] H. A. Stone and L. G. Leal, "Relaxation and breakup of an initially extended drop in an otherwise quiescent fluid," J. Fluid Mech. **198**, 399 (1989).
[43] L. W. Schwartz and R. R. Eley, "Simulation of droplet motion on low-energy and heterogeneous surfaces," J. Colloid Interface Sci. **202**, 173 (1998).
[44] L. W. Schwartz, R. V. Roy, R. R. Eley, and S. Petrash, "Simulation of droplet motion on low-energy and heterogeneous surfaces," J. Colloid Interface Sci. **234**, 363 (2001).
[45] K. B. Glasner, "Spreading of droplets under the influence of intermolecular forces," Phys. Fluids **15**, 1837 (2003).
[46] L. M. Pismen and B. Y. Rubinstein, "Spreading of a wetting film under the action of van der Waals forces," Phys. Fluids **12**, 480 (2000).
[47] J. M. Davis and S. M. Troian, "Influence of attractive van der Waals interactions on the optimal excitations in thermocapillary-driven spreading," Phys. Rev. E **67**, 016308 (2003).
[48] L. M. Pismen and U. Thiele, "Asymptotic theory for moving droplet driven by a wettability gradient," Phys. Fluids **18**, 042104 (2006).
[49] C. A. Perazzo and J. Gratton, "Navier-Stokes solutions for parallel flow in rivulets on an inclined plane," J. Fluid Mech. **507**, 367 (2004).
[50] R. Goodwin and G. M. Homsy, "Viscous flow down a slope in the vicinity of a contact line," Phys. Fluids A **3**, 515 (1991).
[51] A. Münch and B. Wagner, "Contact-line instability of dewetting thin films," Physica D **209**, 178 (2005).
[52] J. H. Snoeijer, "Free-surface flows with large slope: Beyond lubrication theory," Phys. Fluids **18**, 021701 (2006).
[53] G. J. Hirasaki and S. Y. Yang, "Dynamic contact line with disjoining pressure, large capillary numbers, large angles and pre-wetted, precursor, or entrained films," Contact Angle, Wettability and Adhesion **2**, 1 (2002).
[54] A. Oron, S. H. Davis, and S. G. Bankoff, "Long-scale evolution of thin liquid films," Rev. Mod. Phys. **69**, 931 (1997).
[55] G. Teletzke, H. T. Davis, and L. E. Scriven, "How liquids spread on solids," Chem. Eng. Commun. **55**, 44 (1987).
[56] V. S. Mitlin and N. V. Petviashvili, "Nonlinear dynamics of dewetting: Kinetically stable structures," Phys. Lett. A **192**, 323 (1994).
[57] N. Samid-Merzel, S. G. Lipson, and D. S. Tannhauser, "Pattern formation in drying water films," Phys. Rev. E **57**, 2906 (1998).
[58] L. M. Hocking, "The influence of intermolecular forces on thin fluid layers," Phys. Fluids A **5**, 793 (1993).
[59] L. M. Hocking, "The spreading of drops with intermolecular forces," Phys. Fluids **6**, 3224 (1994).
[60] V. S. Ajaev, "Viscous flow of a volatile liquid on an inclined heated surface," J. Colloid Interface Sci. **280**, 165 (2004).
[61] Q. Wu and H. Wong, "A slope-dependent disjoining pressure for non-zero contact angles," J. Fluid Mech. **506**, 157 (2004).
[62] J. Diez and L. Kondic, "Computing three-dimensional thin film flows including contact lines," J. Comput. Phys. **183**, 274 (2002).
[63] R. Seemann, S. Herminghaus, and K. Jacobs, "Dewetting patterns and molecular forces: A reconciliation," Phys. Rev. Lett. **86**, 5534 (2001).
[64] K. B. Glasner and T. P. Witelski, "Coarsening dynamics of dewetting films," Phys. Rev. E **67**, 016302 (2003).
[65] K. B. Glasner and T. P. Witelski, "Collision versus collapse of droplets in coarsening of dewetting thin films," Physica D **209**, 80 (2005).
[66] L. Brusch, H. Kühne, U. Thiele, and M. Bär, "Dewetting of thin films on heterogeneous substrates: Pinning versus coarsening," Phys. Rev. E **66**, 011602 (2002).
[67] N. V. Churaev, "Prediction of contact angles on the basis of the Frumkin-Derjaguin approach," Adv. Colloid Interface Sci. **61**, 1 (1995).
[68] K. K. Mohanty, "Fluid in porous media: Two-phase distribution and flow," Ph.D. thesis, University of Minnesota (1981).
[69] F. Brochard-Wyart, H. Hervet, C. Redon, and F. Rondelez, "Spreading of heavy droplets," J. Colloid Interface Sci. **142**, 518 (1991).
[70] A. L. Bertozzi, G. Grün, and T. P. Witelski, "Dewetting films: Bifurcations and concentrations," Nonlinearity **14**, 1569 (2001).